science.sciencemag.org/content/366/6472/1480/suppl/DC1

Supplementary Materials for

Coherent vortex dynamics in a strongly interacting superfluid on a silicon chip

Yauhen P. Sachkou*, Christopher G. Baker*, Glen I. Harris*, Oliver R. Stockdale, Stefan Forstner, Matthew T. Reeves, Xin He, David L. McAuslan, Ashton S. Bradley, Matthew J. Davis, Warwick P. Bowen†

*These authors contributed equally to this work.
†Corresponding author. E-mail: w.bowen@uq.edu.au

Published 20 December 2019, *Science* **366**, 1480 (2019)
DOI: 10.1126/science.aaw9229

This PDF file includes:

Materials and Methods

1 Experimental details

Our experimental system consists of a whispering-gallery-mode (WGM) microtoroidal optical cavity placed inside a vacuum- and superfluid-tight sample chamber at the base of a closed-cycle ^{3}He cryostat. The sample chamber is filled with ^{4}He gas, with a pressure $P = 70$ mTorr at temperature $T = 2.9$ K. Cooling down across the superfluid phase transition temperature condenses the ^{4}He gas into a few-nm-thick superfluid film, which coats the inside of the sample chamber and the optical microcavity (31). For the ^{4}He gas pressure used in the experiment (70 mTorr) the bulk superfluid phase transition temperature is around 1 K. The experiment is carried out at $T \sim 500$ mK, with a 7.5 nm superfluid film thickness. This film thickness is chosen, because it is found to provide a clean third-sound spectrum that can be read-out optically with high signal-to-noise.

The microcavity is fabricated from a wafer made of a 2 μm thick thermal oxide layer grown atop a silicon substrate. The high-quality thermally grown oxide ensures that both top and bottom surfaces of the fabricated resonator have typically < 1 nm RMS roughness (52), leading to reduced vortex pinning (see section 6). The silica microtoroid is isolated from the silicon substrate atop a silicon pedestal (31). Light from a NKT Photonics (Koheras Adjustik) fibre laser with wavelength $\lambda = 1555.065$ nm is evanescently coupled into a resonator WGM (linewidth $\kappa/2\pi \approx 22$ MHz) via a tapered fibre. Superfluid film motion modulates the effective optical path length for the light confined to the periphery of the microcavity (31, 41). This modulation manifests as fluctuations on the optical phase which are resolved via balanced homodyne detection (New Focus 1817) implemented within a fiber interferometer. The photocurrent is recorded with an Agilent Technologies MSO7104A oscilloscope with a sampling rate of 2 MHz. More experimental details are available in reference (31) and its supplementary information.

1.1 Superfluid film properties

With the film thickness and temperature of the superfluid film given above, the superfluid healing length is much smaller than the film thickness, so that the system resides outside of the regime of BKT superfluidity. However, it is quasi-two-dimensional, since only a handful of Kelvon and z-phonon modes have energy below $k_B T$. Applying the standard Kelvon dispersion

$$\omega = \frac{\kappa k^2}{4\pi} \log\left(\frac{1}{k r_c}\right), \tag{S1}$$

and assuming a lowest wavenumber $k = \pi/d$ for film thickness d, we estimate that approximately six modes have energy below $k_B T$. Similarly, assuming phonons with dispersion $\omega = ck$, we find that the lowest mode propagating in the z-direction (vertical) has energy $\sim 1.5 k_B T$, suggesting perhaps only the lowest transverse mode may be relevant. We note that this classification of the superfluid film as quasi-two-dimensional is consistent with previous experiments on superfluidity in Bose-Einstein condensate (see e.g. (17, 18)).

1.2 Monitoring of the vortex-induced frequency splitting

In order to display the frequency splitting evolution data shown in Fig. 3 of the main text, we record the balanced-detector photocurrent with an oscilloscope. The acquired data consists of 6 consecutive traces, separated by short gaps corresponding to the data saving time. Each trace is 50 s long and contains 100 million points (sampling rate 2 MHz). Each 50 s trace is then broken down into 125 bins, each 0.4 s long. We Fourier-transform each bin in order to obtain $6 \times 125 = 750$ third-sound power spectra, as shown in Fig. S1(A). We fit each tracked sound mode with a double-peaked Lorentzian function in order to acquire the frequency separation between the split peaks, see Fig. S1(C). This allows us to plot the frequency splitting for the five tracked sound modes as a function of time, with 750 time steps during the 360 s experimental decay process.

1.3 Geometric contribution to sound splitting

Small departures from circular symmetry of the resonator, for instance induced by the CO_2 laser reflow process used to form the microtoroid (31), may split the third sound modes even in the absence of vortices in the superfluid film. This geometric splitting (39, 40) of the third-sound modes is analogous to the roughness-induced optical doublet splitting well known in high-Q optical microcavities.

In our experiment, most third-sound modes exhibit some small (< 1 kHz) degree of geometric splitting (31). This splitting is easily distinguishable from vortex-induced splitting, as it is of smaller magnitude, constant in time, and can be determined by observing the native splitting present when repeatedly cycling through the superfluid transition temperature. To account for it, we remove its contribution to the total splitting Δf_{total} in order to isolate the vortex-induced contribution Δf_{vortex} using the following relationship (40):

$$\Delta f_{\text{vortex}} = \sqrt{\Delta f_{\text{total}}^2 - \Delta f_{\text{geo}}^2} \tag{S2}$$

The data presented in Fig. 3 of the main text corresponds to the vortex-induced splitting, with the geometric splitting contribution removed.

2 Third-sound mode identification

Figure S1(A) shows a power spectrum of the microcavity transmitted light, revealing the presence of multiple superfluid third-sound modes. Correct identification of the third-sound modes is important in order to ascertain how each third-sound mode is differently affected by the presence of vortices (39). As we discuss in section 2.1 below, the presence of the pedestal has a negligible effect on the third-sound eigenfrequencies, such that the experimental spectrum can be fitted with the eigenfrequencies of a disk resonator. These are Bessel modes of the first kind, identified by their (m,n) mode numbers, which respectively correspond to the mode's azimuthal and radial order (see section 2.1).

We find that our experimental spectrum can be well reproduced by the eigenfrequencies of a 30 μm radius disk resonator with free boundary conditions and a 7.5 nm film thickness[1], with typical frequency discrepancies on the order of a percent (41). Note that the frequency spacing of higher-order Bessel modes is not harmonic, which allows us to discriminate between free and fixed boundary conditions (41). The 'free' boundary condition requires the radial component of the superfluid velocity to be zero at the boundary, and hence implies no mass flow across the resonator boundary. The 'free' boundary condition is therefore also known as the 'no-flow' boundary condition, consistent with our choice of boundary condition for the vortex flows in Sections 3 and 7.

Rotationally invariant third-sound modes ($m = 0$) are most efficient at modulating the effective optical path length of the resonator (41, 53), and thus generally have the highest optomechanical coupling rate and hence the largest signal-to-noise ratio in the power spectrum. This is indeed what we observe, with the fundamental 'drumhead' (0,1) Bessel mode having the largest signal-to-noise ratio in the experiments, see Fig. S1(A). Rotationally invariant modes, however, cannot be decomposed on the basis of clockwise and counterclockwise propagating modes. As such, we do not expect these modes to display any vortex-induced splitting (39). Again, this is what we observe, with the (0,1) mode remaining unperturbed by the vortex generation process, while the (1,3), (1,4), (1,5), (1,7) and (1,8) modes all exhibit splitting, as seen in Fig. S1(A). Observed power spectral densities and frequency splittings of all these modes at the start of the measurement run, *i.e.* right after the vortex generation process, are shown in Fig. S2.

Note that the circular resonator geometry confines third-sound modes both on its top and bottom surfaces. We have however limited our analysis to the third-sound waves located on the underside of the resonator for two main reasons. First, the third sound waves on the top-surface exhibit a smaller splitting due to the presence of vortices generated on the underside of the resonator near the pedestal, as the flow field generated by these vortices is weaker on the top surface. Furthermore, the laser reflow process used to form the optical microcavity typically leads to an offset of the toroidal ring with respect to the equatorial plane of the disk (54), due to the glass preferentially curling upwards during the melting process. For this reason, the third-sound modes located on the topside of the resonator appear at different frequencies and are typically more shielded from the optical mode and therefore appear with a lower signal-to-noise in the experimental spectra. Peaks around 230 kHz and 315 kHz in the power spectrum of Fig. S1(A) are for instance ascribed to third-sound modes confined to the topside of the resonator.

2.1 Influence of pedestal on third-sound modes

Here we consider the influence of the silica microtoroid's silicon pedestal on the superfluid helium third-sound eigenmodes on the underside of the toroid (2.1), as well as the pedestal's

[1] The film thickness (via its influence on the speed of third-sound) is used as the sole fitting parameter to match the Bessel mode spectrum. The fitted value of film thickness (7.5 nm) is in good agreement with values extracted from the optical cavity frequency shift (31).

influence on the splitting experienced by these third-sound waves (2.1).

Computation of third-sound eigenfrequencies and splittings. In order to compute eigenfrequencies of third-sound modes and their corresponding vortex-induced frequency splittings, we exploit the Finite Element Method (FEM) techniques outlined in reference (39). The essence of these techniques is the following. Superfluid hydrodynamics, described by a system of the continuity and the linearized Euler equations (40, 42), can be exactly mapped to fluid dynamics of an ideal gas. Similarly, the flow field of a quantized vortex, upon applying a simple transformation, is described by Gauss law, and can be exactly mapped to electrostatics. This allows us to compute the dispersive interaction between vortices and sound modes, and therefore the vortex-induced mode splitting, using the finite element tool COMSOL. For the third-sound modes on a disk geometry, which due to their circular symmetry are defined by Bessel functions, the mode splittings can also be estimated analytically, which was used to verify the simulation results.

Mechanical frequency. Using the FEM techniques described just above, we compare the third-sound eigenfrequencies on an annular domain with free-free boundary conditions at the edge of the disk as well at the level of the pedestal, to the eigenfrequencies on a simple disk geometry of same outer radius. The results are summarized in Table S1. The effect of the pedestal on the third third-sound frequencies is negligible, typically less than one percent. This is because the presence of the pedestal does not significantly alter the third-sound eigenmode shapes, as shown for three different eigenmodes in Fig. S3 and discussed in 2.1.

Mode frequency splitting. Similarly, again exploiting the FEM techniques outlined above, we compare the third-sound mode frequency splitting Δf due to a vortex at the center of a disk geometry to the splitting due to a persistent current around the pedestal in an annular domain. The results are also summarized in Table S1. The splitting differences are again small, typically below 3%. For this reason, it is reasonable to neglect the presence of the pedestal and model the underside of the microtoroid as a circular disk resonator, so far as the mechanical eigenmodes and the splitting they experience is concerned. (The presence of the pedestal is taken into account in the kinetic energy calculations discussed in section 7).

Eigenmodes of a disk and annulus. Here we briefly describe the analytical expression of the superfluid third sound eigenmodes. The eigenmodes on a disk are given by (41):

$$\eta_{m,n}(r,\theta) = \eta_0\, J_m\left(\zeta_{m,n}\frac{r}{R}\right)\cos(m\theta)\,, \tag{S3}$$

where $\eta_{m,n}$ describes the out-of-plane deformation of the superfluid surface for the (m,n) mode as a function of polar coordinates r and θ. The (m,n) numbers respectively correspond to the mode's azimuthal and radial order, and $\zeta_{m,n}$ is a frequency parameter depending on the mode order and the boundary conditions. The eigenmodes on an annulus (41) are given by:

$$\eta_{m,n}(r,\theta) = \eta_0 \left(J_m \left(\zeta_{m,n} \frac{r}{R} \right) + \xi Y_m \left(\zeta_{m,n} \frac{r}{R} \right) \right) \cos(m\theta) \tag{S4}$$

Where J_m and Y_m are respectively Bessel functions of the first and second kind of order m. For small values $r_p \ll R$, as is the case in our experiments, $\xi \ll 1$ as Y_m diverges at $r = 0$, and the eigenmodes of the annulus are very close to those of the disk.

3 Dissipative point-vortex dynamics

Here we introduce the dissipative Point Vortex Model (PVM) discussed in the main text. We employ this model in order to:

- Calculate the metastable quasi-equilibrium states of the system (sections 3.2 and 3.5).
- Provide a fit to our experimentally measured vortex decay dynamics and extract the mutual friction coefficient α (also sometimes termed the dissipation coefficient) and diffusion coefficient D (section 3.3).

3.1 Model

The motion of quantum vortices of circulation $\kappa_j = s_j\, h/m$ (with $s_j \in \mathbb{Z}$ the vortex charge) in a thin superfluid film of density ρ_s, thickness d, and temperature T can be described by the equation of motion (55, 56)

$$\frac{\mathrm{d}\mathbf{r}_i}{\mathrm{d}t} = \mathbf{v}_s^i + C(\mathbf{v}_n - \mathbf{v}_s^i) + s_i \left(\frac{D h \rho_s d}{m k_B T} \right) \hat{\mathbf{z}} \times (\mathbf{v}_n - \mathbf{v}_s^i). \tag{S5}$$

Here $\mathbf{v}_n$ is the velocity of the normal fluid and $\mathbf{v}_s^i$ is the local superfluid velocity, evaluated at $\mathbf{r}_i$, excluding the self-divergent velocity field of the vortex at $\mathbf{r}_i$ (56). The parameters C and D are phenomenological mutual friction coefficients, which originate from the scattering of quasiparticles such as phonons, rotons, and ripplons by the vortex cores; these parameters are dependent on temperature, film thickness, and the complex interactions of vortices with defects in the substrate (55, 56). Note that in the absence of friction, a vortex simply moves with the local superfluid velocity, as in the case of ordinary point-vortex dynamics of an ideal fluid (57). The value of the diffusivity D is typically $< \hbar/m$ when operating well below the superfluid transition, as is the case for our experiments (8). The parameter C ranges between 0 and 1.

In our system the normal fluid is viscously clamped to the surface of the microtoroid (31) and we may therefore assume $\mathbf{v}_n = \mathbf{0}$, giving

$$\frac{\mathrm{d}\mathbf{r}_i}{\mathrm{d}t} = (1 - C)\mathbf{v}_s^i - s_i\, \alpha\, (\hat{\mathbf{z}} \times \mathbf{v}_s^i). \tag{S6}$$

where we have defined the mutual friction coefficient $\alpha = (Dh\rho_s d/mk_BT)$. The superfluid velocity $\mathbf{v}_s$ generated by the vortices is determined by the Green's function of the domain (56). Here we approximate the surface of the microtoroid as a hard-walled circular disk of radius R. The velocity at vortex i is thus given in terms of the relative vortex positions as

$$\mathbf{v}_s^i = \frac{1}{2\pi}\sum_{j\neq i}\frac{\kappa_j}{r_{ij}^2}\begin{pmatrix}-y_{ij}\\ x_{ij}\end{pmatrix} + \frac{1}{2\pi}\sum_{j}\frac{\bar{\kappa}_j}{\bar{r}_{ij}^2}\begin{pmatrix}-\bar{y}_{ij}\\ \bar{x}_{ij}\end{pmatrix}, \tag{S7}$$

where $x_{ij} = x_i - x_j$ and, $r_{ij}^2 = x_{ij}^2 + y_{ij}^2$. The barred terms $\bar{x}_{ij} = x_i - \bar{x}_j$, etc. correspond to image vortices with $\bar{\kappa}_j = -\kappa_j$ placed outside the disk at the inverse point $\bar{\mathbf{r}}_i = R^2\mathbf{r}_i/|\mathbf{r}_i|^2$. These fictitious image vortices enforce the boundary condition $\mathbf{v}_s \cdot \hat{\mathbf{n}}|_{r=R} = 0$, i.e. the flow across the boundary is zero at $r = R$.

The kinetic energy of the fluid can be expressed in terms of the relative vortex positions. In a disk of radius R, the vortex Hamiltonian for N vortices with core size a_0, is given by (58, 59)

$$\begin{aligned} H = &-\frac{\rho_s d}{4\pi}\sum_{i<j}^{N,N}\kappa_i\kappa_j \ln\left(\frac{r_{ij}^2}{Ra_0}\right) + \frac{\rho_s d}{4\pi}\sum_{i=1}^{N}\kappa_i^2 \ln\left(\frac{R^2 - r_i^2}{Ra_0}\right) \\ &+ \frac{\rho_s d}{4\pi}\sum_{i<j}^{N,N}\kappa_i\kappa_j \ln\left(\frac{R^4 - 2R^2\mathbf{r}_i\cdot\mathbf{r}_j + r_i^2 r_j^2}{R^3 a_0}\right), \end{aligned} \tag{S8}$$

where $r_i = |\mathbf{r}_i|$. In the absence of friction ($\alpha = C = 0$), H generates the vortex dynamics, described in Eq. (S7), from Hamilton's equations as

$$\kappa_i\frac{\mathrm{d}x_i}{\mathrm{d}t} = \frac{\partial H}{\partial y_i}, \qquad \kappa_i\frac{\mathrm{d}y_i}{\mathrm{d}t} = -\frac{\partial H}{\partial x_i}. \tag{S9}$$

In addition, the angular momentum of the fluid, $L = \int \mathrm{d}^2\mathbf{r}\ (\mathbf{r}\times\mathbf{u})_z$, with velocity field given by $\mathbf{u}$, can be calculated from the position of the point vortices for the case of zero net circulation relevant here as (60)

$$L = -\frac{\rho d R^2}{2}\sum_i \kappa_i r_i^2. \tag{S10}$$

The parameter C is non-dissipative (it does not influence the relative distances between vortices), and therefore does not contribute to the decay of the superflow (55). We therefore set $C = 0$. As shall be addressed later in section 3.3, we measure the mutual friction coefficient to be on the order of $\alpha \sim 10^{-6}$. As the dimensionless parameters α and C originate from similar microscopic processes, we expect that they would be of comparable magnitude, as is indeed the case in bulk superfluid helium (61–63); since $\alpha \ll 1$, the assumption $(1 - C) \approx 1$ is therefore a reasonable approximation.

We add two phenomenological features to the model:

- Pinning of vortices to the pedestal of the microtoroid. In our experiments, we infer a large multi-quantum vortex is pinned to toroid's pedestal. To model this, we assume rigid pinning, forcing Eq. (S6) to equal zero for the vortices pinned at the origin.

- Vortex-antivortex annihilation. Vortex-antivortex pairs in a superfluid annihilate once they approach each other within a distance comparable to the core size (64), which is not included in Eqs. S9. To account for the annihilation of free vortices in the orbiting cluster with quantized circulation of the opposite sign trapped around the pedestal, we remove a free vortex from the simulation when it reaches the radius of the pedestal, $r_p = R/30$, along with one quantum of circulation from the pedestal.

3.2 Metastable states

The description of the vortex distributions in our experiments in terms of metastable states relies on a separation of timescales between the dissipative and coherent dynamics. In this case, the system will sample many microstates on a timescale short compared to the time over which the energy, angular momentum and vortex number change, with the average behaviour (i.e. the metastable state) given by the macrostate with the largest entropy (17, 19, 65). To estimate the characteristic timescale for the coherent dynamics we evolve the conservative ($\alpha = 0$) Hamiltonian dynamics of the cluster and calculate its dipole moment

$$|\mathbf{d}| = \left| \frac{1}{N} \sum_{i}^{N} s_i \, \mathbf{r}_i \right|, \tag{S11}$$

as a function of time. We begin the simulations with a ring of vortices with zero dipole moment. We find that the dipole moment rapidly becomes non-zero as the vortex dipole forms, and asymptotes towards a non-zero value at which point it persists indefinitely. In Fig. S4, we plot the dipole moment for a cluster of 17 negative vortices, initialised initially in rings of varying radius r_0 (so as to easily parametrize the cluster), in the presence of a flow generated by a pinned $\kappa = 17\, h/m$ vortex at the centre of the disk. Due to the chaotic dynamics of the vortices, the rings become disordered over time, evolving towards a horse-shoe shaped distribution characteristic of a metastable state. Figure S4 shows that for all choices of initial radius the dipole moment of each distribution asymptotes to a constant value within a time smaller than $\tau \sim 20$ ms. This value is consistent with the estimation based on the $\tau \sim r_c^2/N\kappa$ formula discussed in the main text.

The system therefore does exhibit the required large separation of timescales between the time for mixing (the cluster turnover time) and the timescales for dissipation (minutes) and annihilation events (tens of seconds). As the dynamics are expected to be chaotic, on intermediate timescales the system will explore many microstates in a narrow band of kinetic energy and angular momentum values at fixed vortex number. It hence approximately realizes the microcanonical ensemble, with only the energy, angular momentum, and vortex number of the initial distribution defining the metastable state. Using this information, we calculate the metastable states over the entire experimentally-relevant parameter space of (N, L, K). We range the vortex number between $N = 2$ to $N = 19$ (as $N = 1$ corresponds to the trivial case where the vortex simply orbits at a constant radius). For each cluster number, we sample ~ 270 points in (L, K) space and simulate the conservative point-vortex model ($\alpha = 0$) for $t \simeq 0.6$ s to ensure the cluster has had enough time to sample the metastable state (c.f. Fig. S4)

We visualize each metastable state by calculating the mean density of vortex positions over the course of the simulation. As the vortices perform many orbits during a simulation, plotting this in a fixed reference frame would produce a doughnut-shaped rotationally invariant-density profile. In order to visualize the angular spread of the orbiting cluster, we instead go into a frame rotating with the vortex cluster: at each time step, we rotate the cluster such that its dipole moment lies along the y-axis (66). An example of this visualisation can be seen in Fig. S5(B).

3.3 Implementation

We solve the system of equations in Eq. (S6) to calculate the motion of vortices with energy damping. We initialize the positions of the 17 negative vortices via a random uniform distribution to form a ring, with the condition that the distribution must have a kinetic energy comparable to the initial energy in the experiment (~ 0.9 aJ). We simulate the dynamics of the system thirty separate times with different initial vortex positions, each constrained by initial energy, with dissipation $\alpha = 0.03$. The total kinetic energy of the system is computed using the Hamiltonian in Eq. (S8). In Fig. 4C&D of the main text, a single simulation result is plotted (solid blue line), with the light-blue shading representing one standard deviation on either side of the mean in the thirty runs.

Since the free vortex cluster evolves slowly through quasi-equilibrium states, we find that the macroscopic dynamics scale with the mutual friction coefficient α, as shown in Fig. S6. Each curve seen in Fig. S6 is an average over 10 runs with different initial conditions. We expect that scaling will improve at lower dissipation rates as the timescale of energy loss will be far smaller than the timescale of coherent dynamics. As such, we choose a value of dissipation that is larger than the experimental one, and scale the results accordingly to best fit the experimental data, rescaling α in the process. This is necessary due to increasingly large simulation times for decreasing α. Within our simulations, we effectively run the system for approximately ~ 50 ms.

3.4 Mutual friction coefficient

After scaling the results from the simulations, we find the experiment is consistent with a mutual friction coefficient of $\alpha \sim 2 \times 10^{-6}$, and hence a diffusion coefficient of approximately $D \sim 1 \times 10^{-16}\ \mathrm{m}^2\ \mathrm{s}^{-1}$. Values of α and D extracted from the second set of measurements (see section 5) are in close agreement, yielding $\alpha \sim 3 \times 10^{-6}$ and $D \sim 1.5 \times 10^{-16}\ \mathrm{m}^2\ \mathrm{s}^{-1}$. Even though the vortices in our superfluid film are quasi-two-dimensional, the observed mutual friction is consistent with observations for bulk helium at the same temperature (45).

We note that Svistunov and Kozik (67) provide an expression for the mutual friction in bulk superfluid

$$\alpha = \frac{\Upsilon}{2\pi} \frac{(k_B T)^5}{\hbar^3 m_{\mathrm{He}} \rho c^7}, \tag{S12}$$

assuming ballistically propagating phonons scattering from a vortex (valid at low temperature/high superfluid fraction), where $\Upsilon \sim 35.368$. Assuming $T = 500$ mK, $\rho = 145$ kg/m^3 and $c \sim 240$ m/s yields $\alpha \sim 2.3 \times 10^{-6}$, close to the values we observe.

While consistent with our observed values, it is unclear to what extent the above formula may be applied to our system, given that we expect most of the vertically-propagating phonon modes and Kelvin modes to be suppressed by the quasi-two-dimensional geometry. Future work, measuring the decay over a range of temperatures, film thicknesses and perhaps varying surface properties, would elucidate the contributions of various mechanisms to the value of mutual friction observed in our system.

3.5 Expanding vortex clusters

For two of the vortex decay models tested in the paper, we are interested in the evolution of expanding vortex clusters, in the one case with no surface interactions, and in the other with dynamics dominated by hopping between surface pinning sites. We would like to know the characteristic distributions of vortices as a function of time in both cases. As it turns out, two types of evolution can be distinguished: 1) evolution towards a common shape of distribution (for the case of no surface interactions, this is a circular distribution with uniform density, while with surface pinning it is a Gaussian), and 2) expansion of that distribution over time. We hope that the evolution in the shape of the distribution occurs at a faster rate than the expansion, to allow simple models of the expansion process (with fixed distribution shape) to be used in further analysis. This turns out to be the case both with, and without, pinning. We would note that the rates of both types of evolution are linearly proportional to the mutual friction coefficient, so that this conclusion is independent of the value of the coefficient.

To study the scenario with no surface pinning, we use the point vortex model described above to observe the evolution of the density distribution of a vortex cluster initialized with a strongly non-uniform distribution. This simulation is used in the following section (4) to test a possible vortex decay scenario. In Fig. S7 we show that the density of a distribution of $N = 1000$ vortices becomes uniform across the disk (despite an initial Gaussian density distribution) on a timescale that is shorter than the timescale of the expansion, i.e. $\tau_{\text{uniform}} < \tau_{\text{expansion}}$. We have performed similar simulations with initial density distributions corresponding to a ring or a flat-top, and observed the same rapid evolution towards uniform density (with respect to the expansion rate). The exact times in Fig. S7 are arbitrary and depend upon the magnitude of the mutual friction coefficient chosen. That being said, the interval between each time is constant.

We next simulate the expansion of a vortex cluster under the influence of pinning sites. These simulations are used in the next section to test an alternate vortex decay scenario. As previously, we begin with a Gaussian density distribution of vortices, but phenomenologically include vortex pinning within the point-vortex model. We model vortex pinning by asserting a mean-free-path,

ℓ, associated to the likelihood of a single vortex becoming pinned. The probability of a vortex remaining unpinned after travelling a distance Δx is assumed to be exponentially decreasing, so that the probability of a vortex becoming pinned is $P(\text{pin}) = 1 - \exp(-\Delta x/\ell)$[2]. Figure S8 shows that the density of a cluster of $N = 100$ vortices remains approximately Gaussian for this situation, but become more spread out over the disk due to energy dissipation.

4 Vortex decay models

Because the frequency splitting experienced by each third sound mode due to the presence of a vortex is unique (see Figure 1 of the main text, and reference (39)), the ability to monitor the splitting on multiple third-sound modes simultaneously allows us to infer spatial information about the experimental vortex distribution. We show here how this capability enables us to discriminate between several different vortex decay scenarios.

4.1 Test of various decay models

We test four different scenarios which may account for the experimentally observed decay of the frequency splitting (see sketches in Fig. S9(A)):

- Scenario 1. The experimentally observed splitting is initially due to a tight cluster of same-signed vortices located at the center of the resonator. Such a distribution could be initialized by a circular stirring of the superfluid film, resulting in a centripetal Magnus force on one sign of vortices. After initialization, dissipation in the system will drive a radial expansion of the tightly-packed cluster. As discussed in section 3.5, point-vortex simulations reveal that a tight vortex cluster will rapidly relax into an expanding flat-top (spatially uniform) distribution, irrespective of the initial cluster arrangement. This flat-top expansion scenario is depicted on the blue resonator in Fig. S9(A).

- Scenario 2. The experimentally observed splitting is due to a tight cluster of same-signed vortices located in the center of the resonator, as in scenario 1. The difference here lies in the presence of pinning sites (black stars) on the resonator surface. Expansion of the tightly-packed cluster in the presence of pinning sites resembles diffusive Brownian motion whereby vortices hop from pinning site to pinning site with a slow outward drift due to dissipation (see individual vortex trajectory marked by black arrows). Under such conditions the spatial probability density distribution of the expanding cluster can be approximated by a Gaussian (see section 3.5 for further details and point-vortex simulations). This Gaussian expansion scenario is depicted on the green resonator in Fig. S9(A).

[2]This simple model assumes an infinite pinning potential, such that once pinned, a vortex is permanently immobilized. Other simulations with a critical pinning velocity below which a vortex gets pinned, which allow for multiple pinning and unpinning events for each vortex, yield qualitatively similar results.

- Scenario 3. The experimentally observed splitting is due to a macroscopic persistent current around the pedestal at the center of the resonator (see discussion of the pinning potential due to the pedestal in section 7). This persistent current then decays through the slow shedding of same-sign vortices. Due to dissipation, these vortices will rapidly spiral out of the resonator, such that the probability density can be modelled by a temporally decaying delta function in the center of the resonator. This persistent current decay scenario is depicted on the orange resonator in Fig. S9(A).

- Scenario 4. The experimentally observed splitting is due to a macroscopic persistent current pinned by the pedestal at the center of the resonator, and a cluster of orbiting free vortices of opposite sign. Such a distribution can be initialized by a superfluid flow exceeding the critical velocity up the device pedestal, leading to the generation of pairs of opposite-sign vortices. One sign pins to the pedestal while the other forms into a freely orbiting cluster. After initialization, dissipation will cause the orbiting cluster to spiral inwards, where it will annihilate with the persistent current on the pedestal. This vortex dipole decay scenario is depicted on the purple resonator in Fig. S9(A).

Each decay model is tested by comparing its predicted splitting on all third-sound modes to the experimental data. The results of this comparison are shown in Fig. S9(B), which shows that the vortex dipole model (Scenario 4) provides the best fit to the data. Vortex cluster expansion due to both vortex-vortex interactions and diffusive hopping fit the data poorly at all times. Vortex shedding fits the data at long times, but does not well fit the initial vortex distribution. We note that vortex shedding is also unlikely from a physical perspective due to the strong potential energy barrier for the process due to the pedestal, which we estimate to be many hundreds of times larger than the thermal energy (see section 7.2).

We discuss here the flat-top decay model as an example of how the RMS error is calculated. The flat-top distribution is uniquely characterized by an initial vortex number and distribution radius. Looking at the initial splitting of the five tracked third-sound modes, we find the combination of vortex number and distribution radius which most closely matches the experimental results, and the associated confidence intervals, as illustrated in Fig. S10. This initial vortex number is then kept constant throughout the fitting procedure, as the distribution expands with no annihilation events. At all subsequent experimental time steps, the optimal radius which minimizes the RMS error is inferred. The fitting procedure thus produces an estimate of the distribution radius versus time, as well as an RMS error of the fitting procedure versus time, as plotted in the blue trace in Fig. S9(B). The calculation of the RMS error for the other decay scenarios follows a similar approach. In scenario 3, the optimization is performed over N, the number of circulation quanta around the pedestal. In the vortex dipole decay case (purple), since the vortex number is also no longer constant due to annihilation events, the optimization at every time step occurs over a three-dimensional space (vortex number, angular momentum and kinetic energy), as in the initial fitting step of the flat-top distribution shown in Fig. S10.

All scenarios start with a tightly-packed initial vortex distribution or macroscopic circulation at the center of the resonator. This is both because we expect the stirring process to generate vortices at the top of the pedestal, where the superflow is fastest, and because the initial ratio of the measured experimental splittings Δf_{exp} closely matches the theoretical splitting Δf_{th} ratios expected from vortices positioned in the center of the resonator:

$$\frac{\Delta f_{\mathrm{exp},\,m}\,(t=0)}{\Delta f_{\mathrm{exp},m'}\,(t=0)} \simeq \frac{\Delta f_{\mathrm{th},\,m}\,(r=0)}{\Delta f_{\mathrm{th},m'}\,(r=0)} \tag{S13}$$

Here the subscripts m and m' refer to different third-sound mode azimuthal orders, and $\Delta f_{\mathrm{th}}\,(r)$ refers to the theoretically calculated vortex-induced splitting functions, as shown in Fig. 1 of the main text. These splitting functions are independently obtained through Finite Element Method (FEM) calculation of the overlap between the vortex and third-sound flow fields (39).

We note that while all scenarios predict a decaying splitting of all third-sound modes, as observed in the experiments, their relative influence on different third-sound modes is quite significant. This is striking in Fig. S9C(*ii*) & S9C(*iii*), which show the predicted splitting on all five third-sound modes at the times marked by the dashed grey lines in Fig. S9(B). We see that both expanding cluster scenarios (flat-top in blue and Gaussian in green) predict similar splitting on all third-sound modes —on the order of 0.8 kHz in (*ii*) and 0.3 kHz in (*iii*)— as the cluster expands. This is in strong disagreement with the experimental data (black squares) for which the splitting is an increasing function of mode number. This mismatch, visible in the much larger RMS errors for these decay scenarios in Fig. S9(B), illustrates how the ability to track the frequency splitting of multiple third-sound modes simultaneously, combined with the linearity of the velocity field contributions due to each vortex, enables us to infer spatial information on the experimental vortex distribution. We observe that the vortex-dipole scenario discussed in the main text (purple) systematically provides the best agreement with the experimentally measured splitting throughout the entire decay process.

4.2 Metastable states of the vortex dipole

Following the data analysis approach described in Section 4.1, we determine temporal dynamics of all three parameters uniquely characterizing vortex dipole distributions. The evolution of the kinetic energy and free-vortex number of the metastable states are shown in Fig. 4A&B of the main text. Here we additionally provide the temporal evolution of the angular momentum. As can be seen in Fig. S11, the angular momentum is constrained less well than either of the other two parameters and is therefore not included in the main text.

5 Second set of measurements

In order to test the reproducibility of the vortex ensemble behaviour, we perform a second set of measurements under similar experimental conditions as in the first run described in section 1. In order to do this, we warm up the cryostat above the superfluid transition temperature (~ 1 K) and then cool the system down back to $T \sim 500$ mK for consistency with the first set of measurements. Recording the balanced-detector photocurrent, we acquire five consecutive time traces carrying information about the superfluid mechanical modes spectrum. In this experimental run, each trace is 20 s long and contains 40 million points (sampling rate 2 MHz). Slicing each 20 s trace into 50 bins (each bin is 0.4 s long) and taking a Fourier transform of each bin, we obtain $5 \times 50 = 250$ third-sound power spectra. In order to compare this set of measurements with the first one, we track the same five third-sound modes – $(m, n) = (1, 3)$, $(1, 4)$, $(1, 5)$, $(1, 7)$ and $(1, 8)$ – and plot their frequency splittings as a function of time (Fig. S12A). We then perform the analysis of these traces as described in section 4.1 and extract all three parameters characterizing the vortex dipole metastable distributions: vortex number, kinetic energy, and angular momentum, shown in Figs. S12A, B, and C respectively. The vortex dipole is initialized with an initial free-vortex number of $N = 33^{+2}_{-1}$. Consistently with the first set of measurements, the total kinetic energy of the vortex dipole continuously decays with time, while the free-vortex kinetic energy increases, which is indicative of evaporative heating (Fig. S12C). Similarly to the first experimental run, the second set of measurements does not constrain the angular momentum well, Fig. S12D.

6 Vortex pinning on surfaces

The presence of surface roughness on a substrate that is in contact with superfluid helium limits the ability of vortices to move freely. Indeed, in thin superfluid films, strong pinning sites can freeze out vortex motion altogether (42). For example, surface roughness is thought to be the primary cause of discrepancy between measurements of the vortex diffusivity around the BKT transition (8). It is for this reason that studies of vortex interaction, dissipation and diffusion are critically dependent on surface quality.

The effect of surface roughness on vortex motion can be understood by considering the case of a superfluid film residing on a smooth substrate with a defect in the form of a hemispherical protuberance, as shown in Fig. S13(A) (68, 69). From this simple picture, one can see that a vortex confined to the defect will be in an energetically favourable state. Indeed, for a constant film thickness d, a vortex located on the defect (center) will have less kinetic energy than one located off the defect (right) due to its shorter length. This energy difference is associated to a trapping potential, which naturally will grow with increasing defect size. Similarly, from this simple picture one can see that for a given defect size, a thick film will lead to weaker pinning, as the height difference introduced by the defect becomes proportionately smaller. In bulk systems, the inclusion of vortex-boundary interactions is thought to be crucial in accurately describing the intriguing phenomena of superfluid turbulence (70–73). In many of those experiments, side-wall roughness is much larger than the angstrom scale of the vortex core (71, 74). However, vortices may depin themselves through large amplitude Kelvin wave excitations (74), or be partially shielded from the roughness by a vortex "mesh", consisting of a dense set of short half-loops connected to the sidewall (70).

In superfluid films, depinning occurs when the forces acting upon the vortex due to the background flow exceeds the strength of the pinning potential. Clear signatures of depinning in superfluid films of thickness $3\,\mathrm{nm}$ have been reported, for example, in Ref. (42). In that experiment, the frequency splitting of degenerate third sound modes is slightly reduced when "stirring" at flow velocities above $150\,\mathrm{cm/s}$, but below the superfluid critical velocity. The observed change in splitting corresponds to depinning of only a small fraction of the total number vortices, namely $10^2 - 10^3$ compared to 10^5, respectively. This observation suggests that those liberated vortices were attached to weak pinning sites, while the remaining vortices were pinned to much stronger pinning sites, which may be consistent with the comparatively larger surface roughness of their evaporated gold substrate.

Here, we ascribe the lack of any apparent contribution of pinning to the vortex dynamics to the combination of an atomically smooth surface and a relatively thick superfluid film. It is conceivable that the mechanisms which suppress pinning in bulk systems, mentioned above, may also be present here. However, those mechanisms are thought to rely on non-trivial vortex deformations, and for the film thicknesses considered here the vortices will be mostly orientated vertically, with only a small number of low-order Kelvin modes thermally excited. Furthermore, any vortex loops created out of equilibrium (i.e. during vortex generation) will be energetically unfavorable and are likely to quickly dissipate compared to the timescales of the experiment.

As discussed in sections 3 & 4 and Fig. 4 of the main text, our data supports a model for vortex motion that is characterized by the decay of a vortex dipole down to a few remaining vortices after a period of minutes. As the vortex dipole decays, the background flow velocity across the disk decreases, as illustrated in Fig. S13B. The observed decay is consistent with point-vortex modelling in the absence of pinning sites (see section 3), suggesting that pinning does not play a significant role in vortex dynamics in this system. Towards the end of the experimental run, the background flow induced by two vortices pinned to the pedestal creates flow velocities below $\sim 0.2\,\mathrm{cm/s}$ over the majority the disk surface. Indeed, the free vortex cluster explores these outer-parts of the disk because, as discussed in the main text, upon an annihilation event the cluster moves towards the periphery. These very low depinning velocities correspond to extremely small surface defects, likely to be of comparable size to the vortex core, consistent with the expected atomic-scale roughness of our commercially purchased silicon wafers.

7 Pinning potential of the pedestal

While superfluid flow is purely irrotational, a superfluid may contain a macroscopic circulation around a hole in the film (75, 76). This hole may take the form of an Angstrom-sized normal fluid core in ^{4}He, or a macroscopic barrier in a non-simply connected geometry. The kinetic energy E_k associated with such a flow around a centred circular hole in a circular domain of radius R is given by:

$$E_{k,n} = \frac{1}{2}\rho_s \frac{(N\,\kappa)^2}{2\pi} \ln\left(\frac{R}{a_0}\right), \tag{S14}$$

with ρ_s the superfluid surface density, a_0 the hole radius and $N \times \kappa$ the quantized circulation around the hole, where $\kappa = h/m_{\mathrm{He}} = 9.98 \times 10^{-8}\,\mathrm{m}^2\ \mathrm{s}^{-1}$ is a single circulation quantum in ^{4}He. Because circulation around a macroscopic barrier – such as the microtoroid pedestal ($a_0 = r_p \sim 10^{-6}$ m) – clips the high-velocity region of the flow (see Fig. S14), it is energetically favourable compared to circulation around a vortex core in the film ($a_0 \sim 10^{-10}$ m). This has been observed in the stirring of superfluids in annular containers, where the vorticity preferentially takes the form of persistent flow around the inner annular boundary, and vortices appear in the fluid itself only for much larger rotation speeds (77, 78).

For our $R = 30$ micron resonator, with pedestal radius $r_p \sim 1\ \mu$m, there is approximately three times less energy in the flow for quantized circulation around the pedestal than around a normal fluid core[3]. However, placing increasingly large circulation around the pedestal becomes less advantageous as the energy cost of each additional circulation quantum $E_{k,N+1} - E_{k,N}$ is boosted by $2\,N$, with N the number of quanta already present, as shown in Equation (S14). This thereby provides an upper bound on the number of circulation quanta around the pedestal before it becomes energetically favourable to shed these and form vortices in the fluid. In order to quantitatively estimate the metastability of the pinning around the pedestal, we numerically calculate the kinetic energy barrier for the shedding of vortices.

7.1 Flow-field calculation

There are two mechanisms through which the large quantized circulation may decay. First, through the escape of vortices of the same sign as the circulation. Second, a negative vortex may be generated at the resonator boundary and migrate inward, annihilating circulation on the pedestal. We estimate the change in kinetic energy of the flow for these two processes.

The streamfunction Ψ_{free} of a point-vortex on the underside of the toroid can be approximated in cartesian coordinates by (39, 65, 79, 80):

$$\begin{aligned}\Psi_{\text{free}} \simeq \frac{\kappa}{2\pi}\Bigg(&\ln\left(\sqrt{(x-X_1)^2+y^2}\right) - \ln\left(\sqrt{(x-X_2)^2+y^2}\right) \\ &+ \ln\left(\sqrt{x^2+y^2}\right) - \ln\left(\sqrt{(x-X_3)^2+y^2}\right)\Bigg).\end{aligned} \tag{S15}$$

Here X_1 is the radial coordinate of the vortex (along the x axis), $X_2 = r_p^2/X_1$ is the radial coordinate of the opposite circulation image-vortex required to enforce no flow across the pedestal boundary and $X_3 = R^2/X_1$ is the radial coordinate of the opposite circulation image-vortex required to enforce no flow across the resonator boundary, as shown in Fig. S15. Because there are two boundaries in the problem, these image vortices also require their own image vortices, leading to an infinite series. However, for small values of $r_p \ll R$, as is the case in our experiments, the infinite series can safely be truncated after the first term, as in Eq. S15, while conserving the absence of flow through the resonator and pedestal boundaries, as visible in the calculated streamlines in Fig. S16(A) and (B). The streamfunction Ψ_{pedestal} of the quantized

[3]The kinetic energy of a centred normal-fluid core vortex on a disk of radius $R = 30\,\mu$m is $\sim 1 \times 10^{-20}$ J, which corresponds to $\sim$2000 $k_B\,T$ (for $T = 500$ mK and a 10 nm thick film).

circulation around the pedestal is given by:

$$\Psi_{\text{pedestal}} = \frac{N\,\kappa}{2\pi}\,\ln\left(\sqrt{x^2+y^2}\right), \tag{S16}$$

with N the number of circulation quanta. The total streamfunction Ψ_{tot} describing the combined flow is then simply $\Psi_{\text{tot}} = \Psi_{\text{free}} + \Psi_{\text{pedestal}}$. From the streamfunction Ψ_{tot}, the superfluid velocity components are given by:

$$v_x = \frac{\partial \Psi_{\text{total}}}{\partial y}; \qquad \text{and} \qquad v_y = -\frac{\partial \Psi_{\text{total}}}{\partial x} \tag{S17}$$

The kinetic energy of a given flow field is obtained through numerical integration of the calculated field (Eq. S17) over the annular region contained within $r_p < r < R$.

7.2 Metastability of the pinned flow around the pedestal

Figures S16(A) and S16(B) illustrate two alternate decay scenarios for a large circulation trapped around the device pedestal. First, a positive vortex (red) can be shed from the large positive pinned circulation around the central pedestal. Second, a negative incoming vortex (blue) can annihilate with the positive circulation on the device pedestal. The energy cost of both these scenarios is illustrated in Fig. S16(C). The red curve plots the energy difference between the two following configurations:

- a positive circulation of 10κ on the pedestal and a point vortex of circulation κ at radial coordinate x
- a positive circulation of 11κ on the pedestal

If the point vortex can move far enough away from the pedestal, this escape process is energetically favourable ($\Delta E < 0$), as the flow fields of the point vortex and the macroscopic circulation no longer sum up constructively. However, as shown in Fig. S16(D), there is an initial energy barrier on the order of several hundred $k_B T$ to do so. Indeed, in the initial stage of the vortex shedding process the flow fields of the pinned circulation and the point vortex still add up constructively, and do not offset the additional energy cost of the high velocity flow near the normal fluid core, as shown in Fig. S14.

As discussed previously, the overall shape of the energy barrier for a single quanta will be dependent on the number of pinned circulation quanta N. For increasing circulation around the pedestal the barrier becomes narrower and shallower (dashed red line in Fig. S16(D)), but the conclusion remains identical. While the lowest energy state of the system corresponds to no persistent current, a large energy barrier (on the order of several hundred $k_B T$ for the vortex numbers present in the experiment) explains why the circulation remains pinned around the device pedestal for the duration of the experiment.

Similarly, the creation of a negative vortex on the device boundary also incurs a large energy penalty due to the energy cost of the high-velocity region near the vortex core (see Fig. S16(C)).

Note however that for radial coordinates $r < 18\ \mu$m, that energy cost is more than offset by the cancellation of the pinned persistent current flow field, such that the negative point-vortex reduces the kinetic energy to the system.

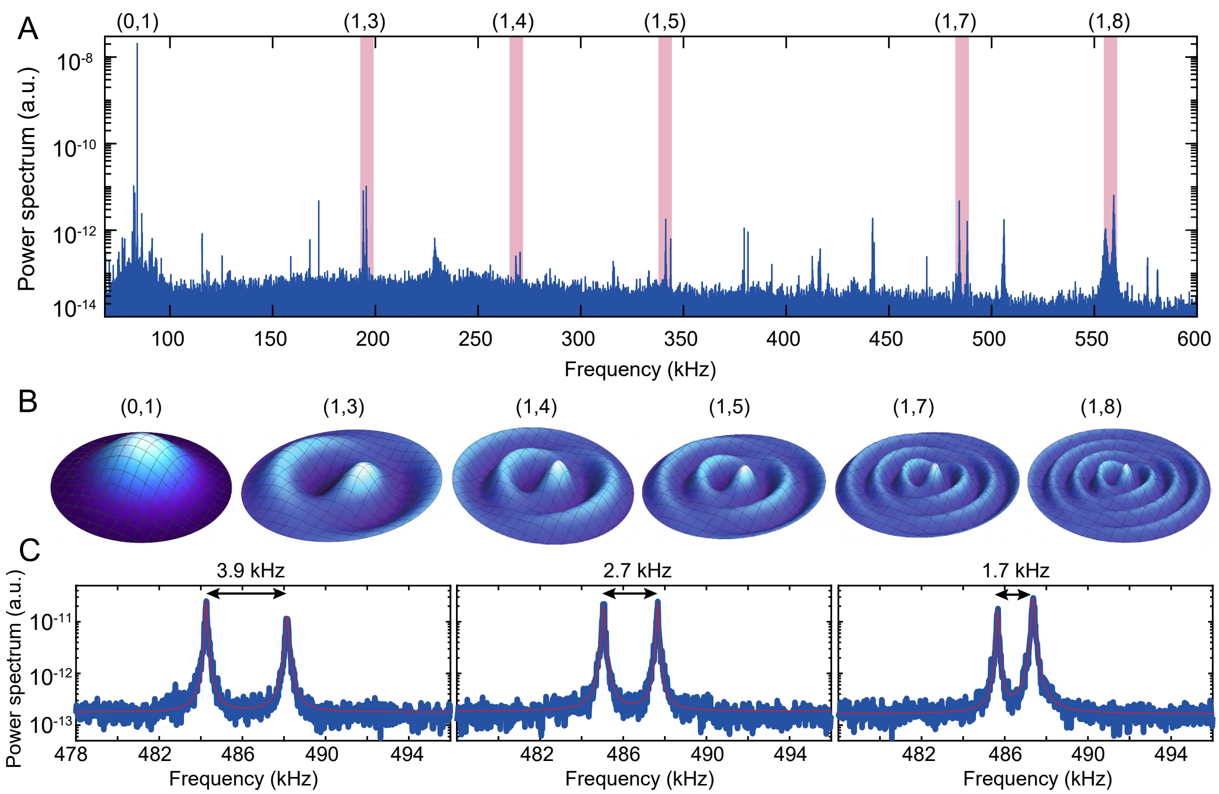

Figure S1: **(A)** Third-sound power spectrum. The five third-sound modes monitored in the experiments are highlighted in red. The red bars are positioned at the theoretically predicted third-sound eigenfrequencies of a 30 μm radius disk resonator with free boundary conditions and a 7.5 nm film thickness (41), in good agreement with the experimental frequencies. Note that mode (1,6) is not used in the experiments, as its proximity to another third-sound mode precludes reliable peak fitting. **(B)** Surface deformation profiles of the six third-sound modes labelled in (A). **(C)** Example of the mode splitting decay observed in the experiments. The three panels show, from left to right, the splitting decay of mode (1,7) as the experiment progresses. Red line: double Lorentzian peak-fit to the data.

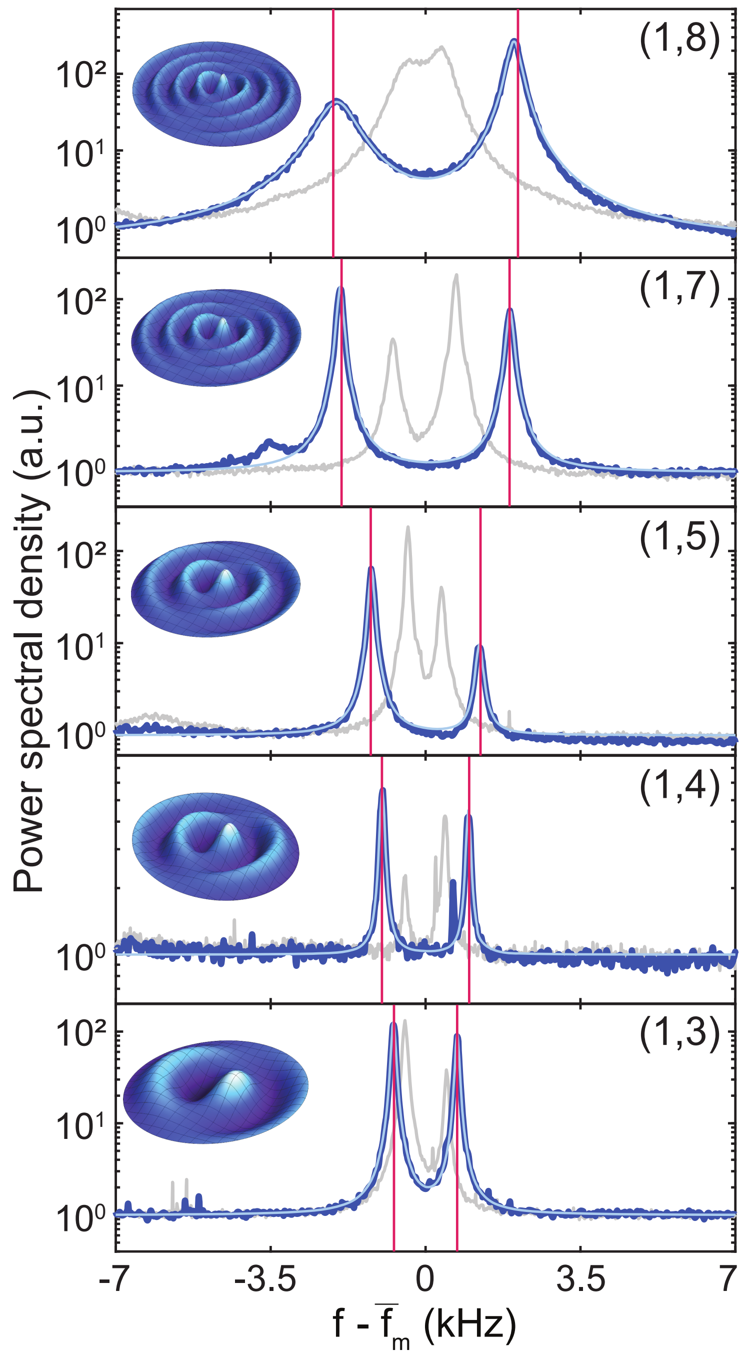

Figure S2: Splittings of $(m, n) = (1, 3)$, $(1, 4)$, $(1, 5)$, $(1, 7)$ and $(1, 8)$ third-sound modes immediately after the vortex generation process. Spatial amplitude profiles of the split modes are shown as insets. Red bars mark the theoretically computed splittings right after the system initialization. Grey spectra correspond to the unperturbed third-sound modes with no vortices present in the system. The residual splitting in these unperturbed spectra is due to irregularities in the circularity of the microtoroid that break the degeneracy between standing-wave Bessel modes (31). We accounted for these in data processing (section 1.3). f: frequency of superfluid motion; $\bar{f}_m$: mean resonance frequency of third-sound mode pair.

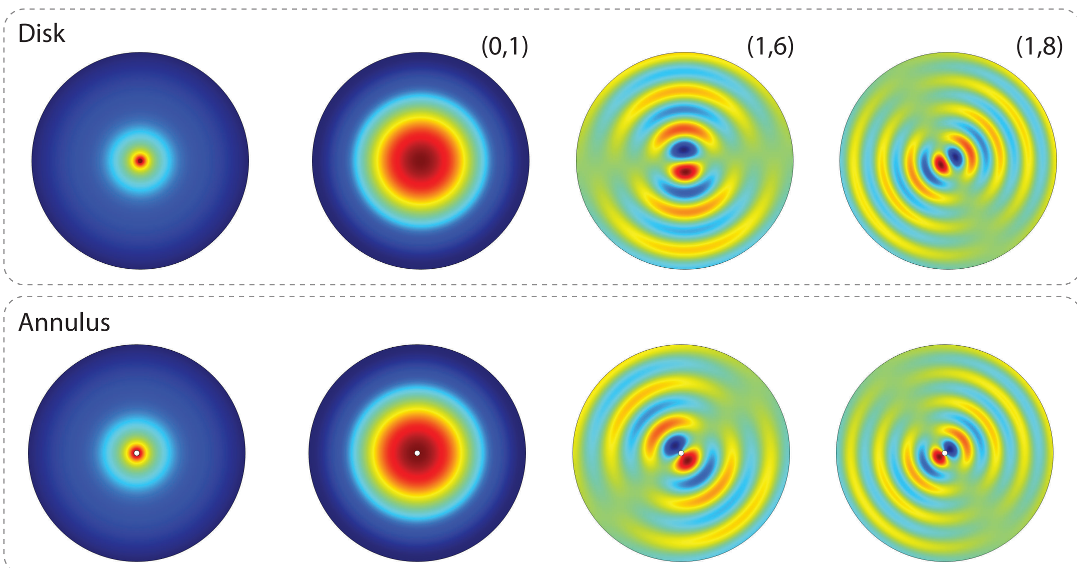

Figure S3: Leftmost image for both disk and annulus: calculated flow field due to quantized circulation around a centered point-vortex (disk) or a persistent current around a pedestal with a 1.5 μm diameter (annulus). Rightmost images: Out-of-plane displacement profile for three distinct third-sound eigenmodes. Color code: Red=positive; blue=negative; green=no displacement. The (m,n) numbers respectively correspond to the mode's azimuthal and radial order, see Eqs. (S3) and (S4) in 2.1.

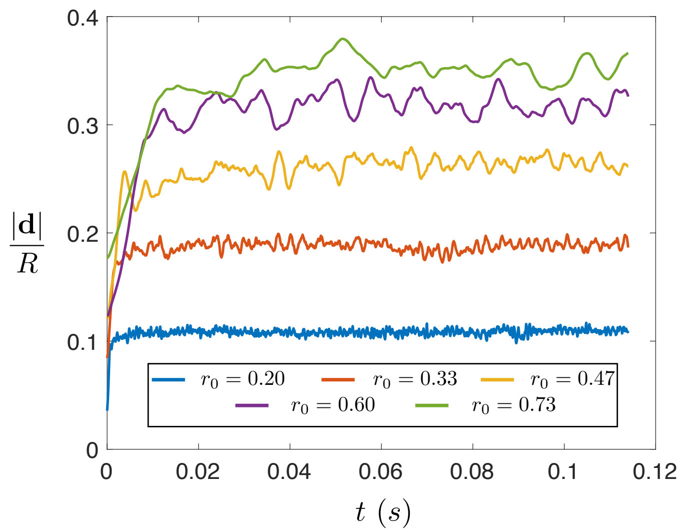

Figure S4: Dipole moment of $N = 17$ vortex cluster, for vortices initialized in a ring formation of varying initial radius r_0. Each curve represents an average of 50 PVM simulation runs. The ring initialization radius r_0 is given here as a fraction of the disk radius R.

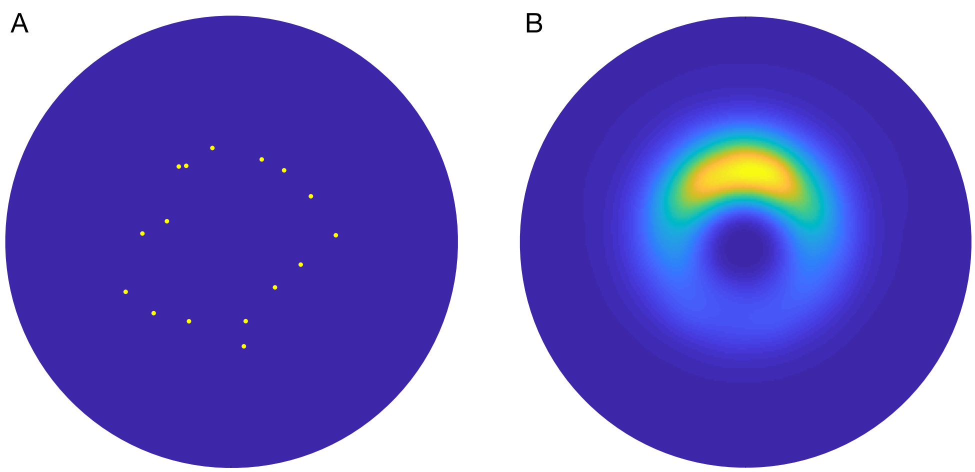

Figure S5: **(A)** Sample initial ring distribution where $N = 16$. Yellow dots correspond to the free vortices in the system, which orbit around the pinned circulation in the center of the resonator (not shown here). **(B)** Time-averaged metastable state over the entire simulation. At each time step, the vortex cluster has been rotated such that the dipole moment lies along the y-axis.

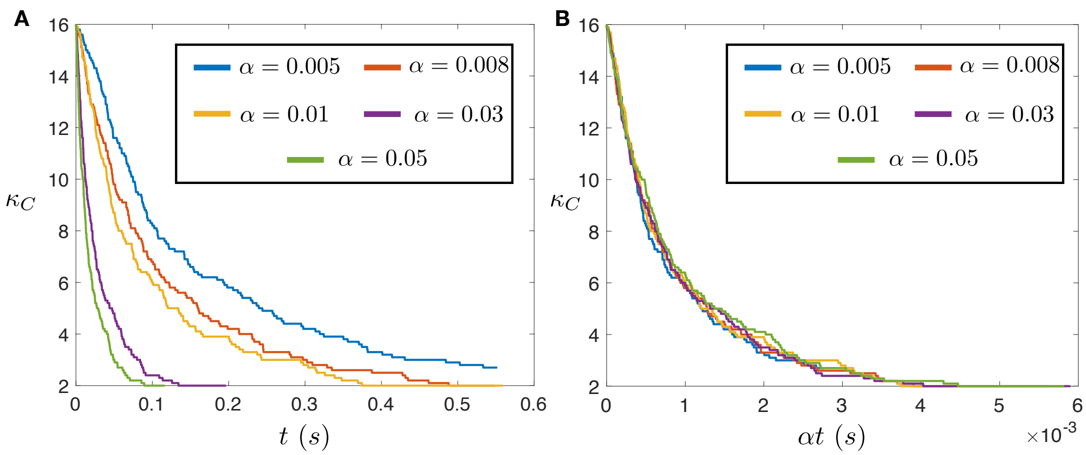

Figure S6: **(A)** Decay of the charge of the pinned multi-quantum vortex (κ_C) for the different mutual friction coefficients given in the legend. Each curve represents the average of 10 runs with different initial conditions constrained by the energy of the cluster. Due to the averaging over the runs, the decay of the central vortex becomes continuous, unlike in a single run where it would be quantized. **(B)** Decay of the charge of the pinned multi-quantum vortex (κ_C) as in (A), but here the time axis has been scaled by the mutual friction coefficient α. The collapse of the data onto a single curve under rescaling of t to αt demonstrates the direct linear scaling of the dynamics with α, allowing the experimental α to be inferred by a rescaling of time.

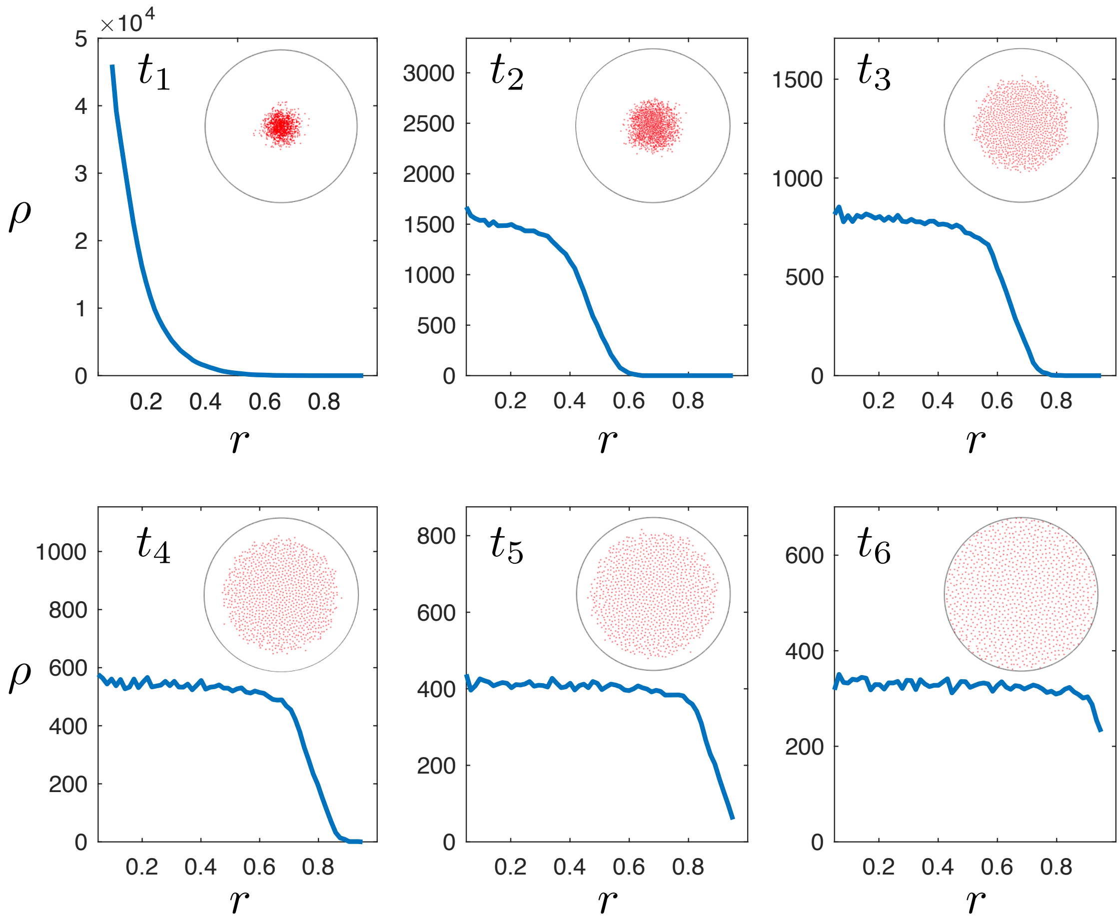

Figure S7: Vortex cluster ($N = 1000$) expansion from an initial Gaussian density distribution. Time progresses from left to right, top to bottom in equal intervals as per the labels. Despite the non-uniform initial distribution, vortices arrange themselves in such a way that the cluster rotates as a rigid body, resulting in an approximately uniform density at later times. This is supported by the insets in each figure, which show the physical position of vortices in the disk tending towards a uniform density.

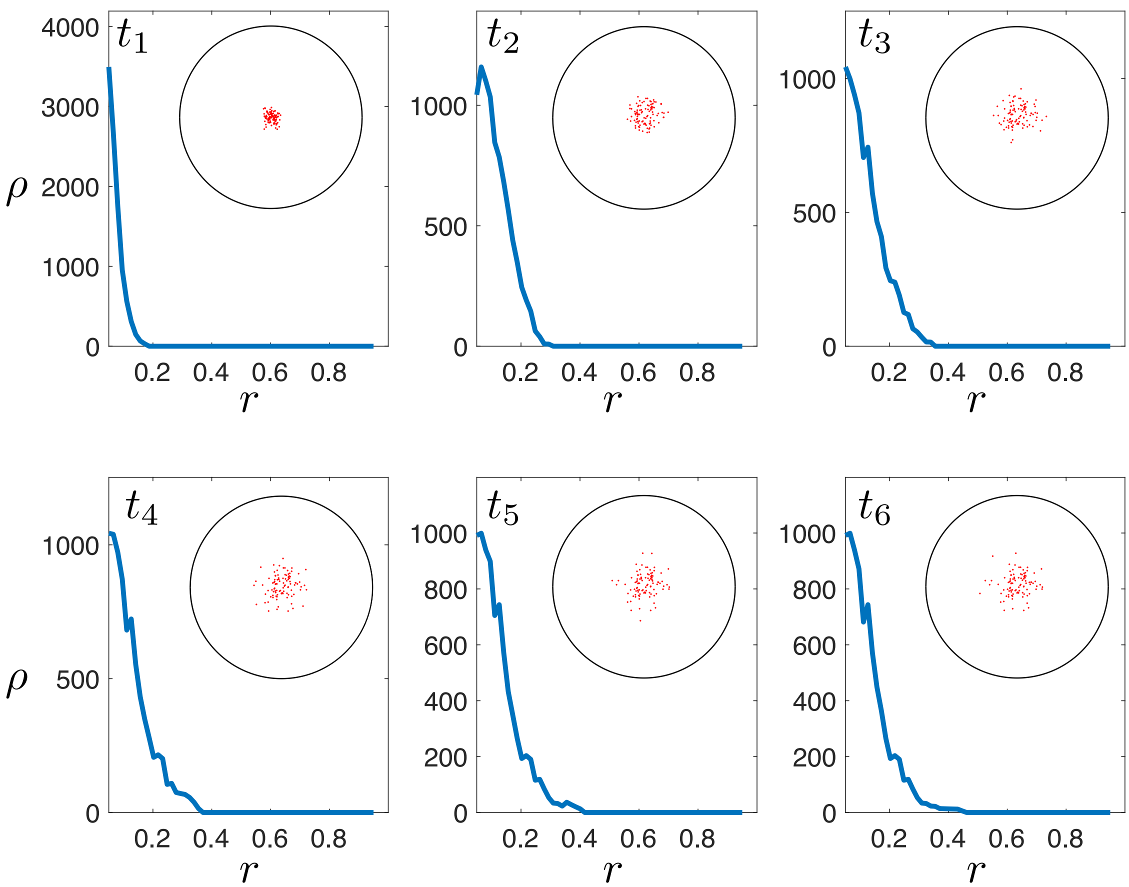

Figure S8: Vortex cluster ($N = 100$) expansion from an initial Gaussian density distribution with vortex pinning. Time progresses from left to right, top to bottom in equal intervals as per the labels. The pinning qualitatively changes the dynamical evolution of the cluster compared to the no-pinning case (Fig. S7). The Gaussian density profile remains approximately Gaussian throughout the simulation, with the standard deviation of the distribution gradually increasing due to damping. Note that by t_4, the cluster is essentially no longer expanding. The choice of the mean-free-path l sets here the maximal cluster width before the vortices freeze out.

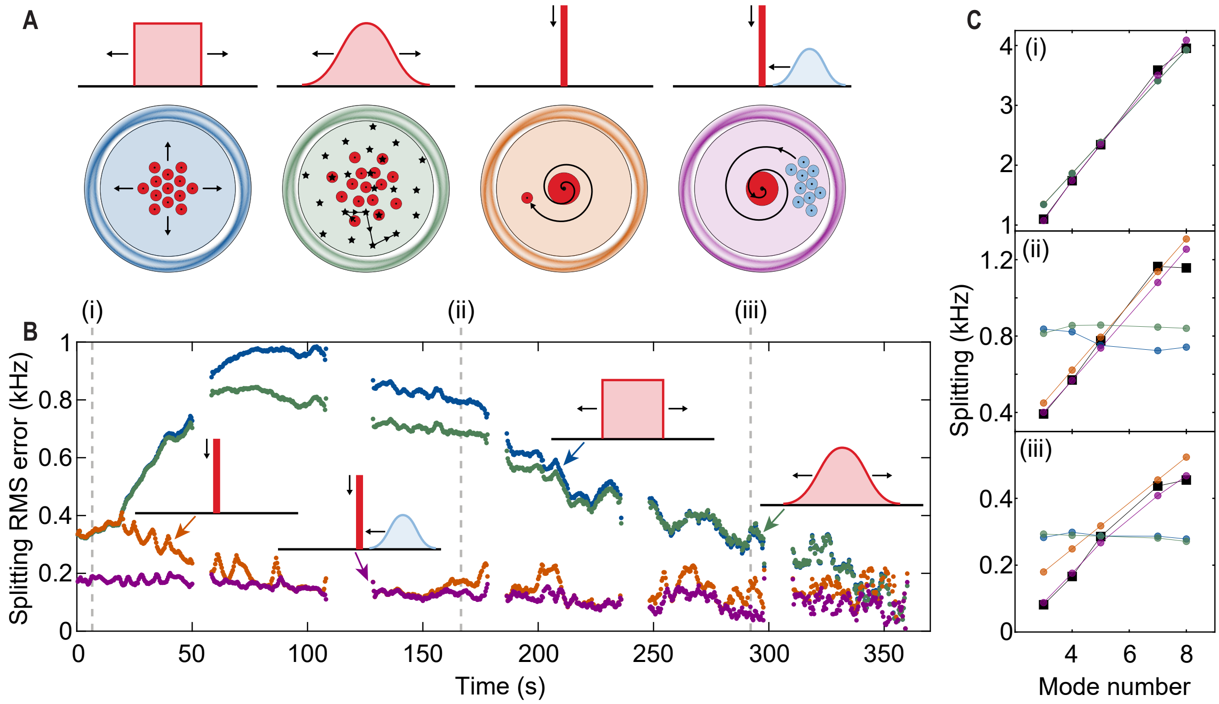

Figure S9: **(A)** Four different vortex decay scenarios. From left to right: flat-top (uniform density) expansion of a vortex cluster (blue disk); Gaussian expansion of a positive vortex cluster with pinning sites (green disk); decay of a macroscopic circulation through shedding of same-sign vortices (orange disk); decay of a macroscopic vortex dipole consisting of a pinned macroscopic circulation (red) and a cluster of free opposite-sign vortices (purple disk). The associated probability density is plotted above each scenario, with the arrows indicating the evolution over time of each distribution. The down arrows represent the reduction in macroscopic circulation due to annihilation events, while the other arrows represent changes in the vortex distribution due to dissipation. **(B)** Calculated RMS error of each decay scenario across the 360 s experimental duration. The trace colors keep the same color scheme as in (A). At longer times, all scenarios converge towards a similar error as the experimental splitting has almost entirely decayed and our approach loses its discriminating power. **(C)** Experimentally-measured splitting of the five tracked third-sound modes ((1,3), (1,4), (1,5), (1,7) and (1,8)) (black squares) and simulated splitting corresponding to the four decay scenarios listed above. Each scenario is identified by the same color code as in (A). Each third-sound mode is identified by its azimuthal mode number m, *e.g.* '8' corresponds to mode (1,8). Plots *i*, *ii* and *iii* correspond to the times indicated by the dashed grey lines in (B).

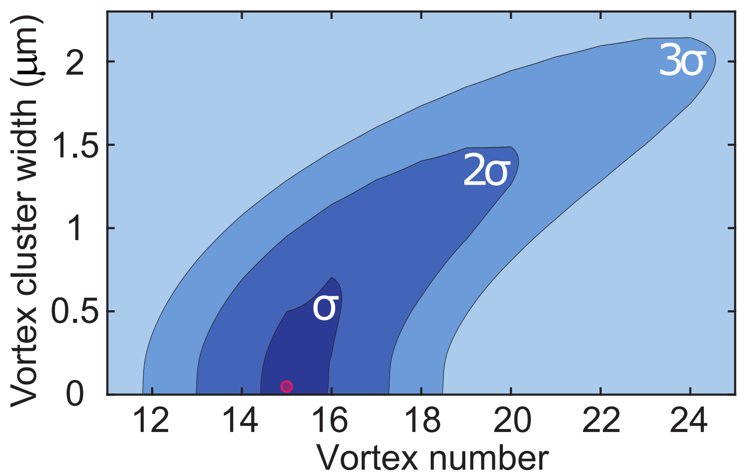

Figure S10: RMS error map for the flat-top distribution decay scenario, computed at $t = 0$. The labeled shaded regions correspond to the one-, two- and three-σ standard deviation confidence intervals. The best fit to experiment at t=0 is provided by 15 vortices near the disk origin in this scenario (red circle).

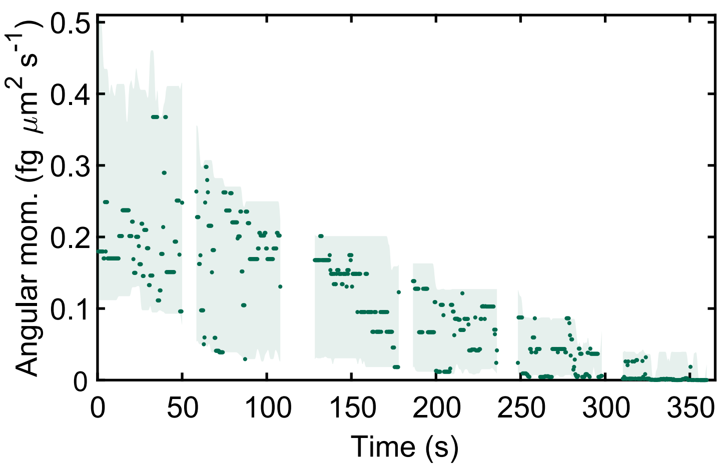

Figure S11: Evolution of the angular momentum of vortex-dipole metastable states.

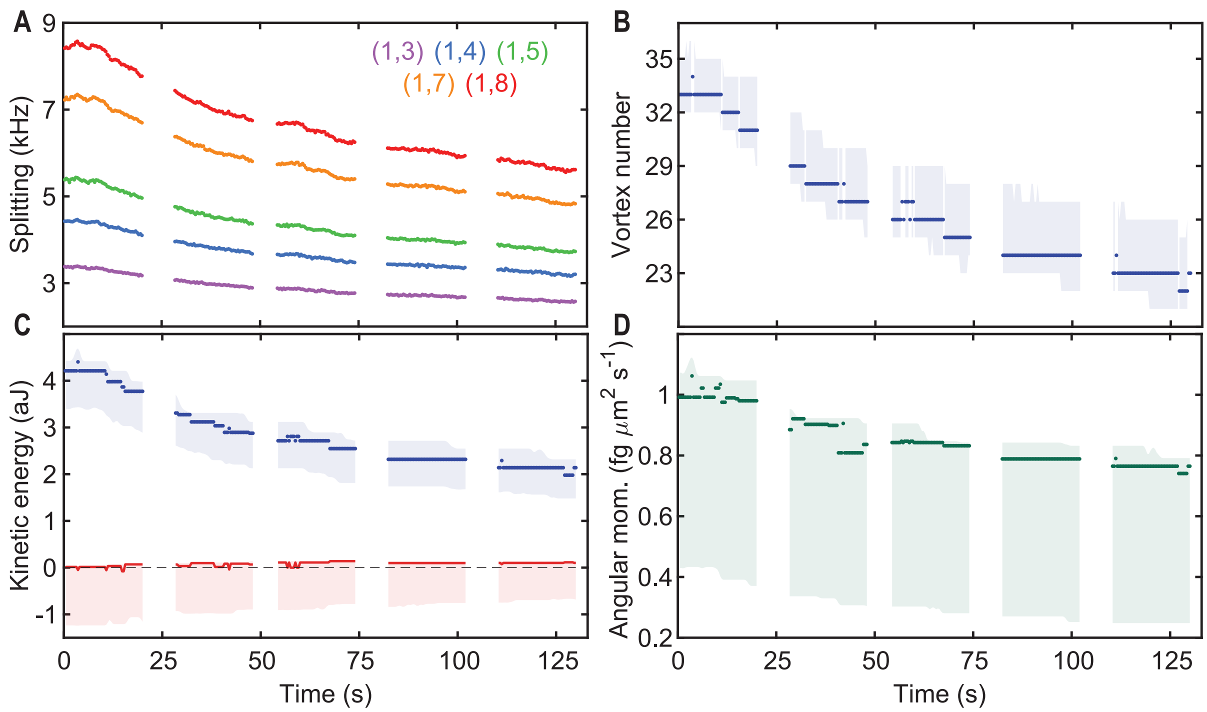

Figure S12: **(A)** Temporal decay of splitting of the $(m, n) = (1, 8)$, $(1, 7)$, $(1, 5)$, $(1, 4)$ and $(1, 3)$ third-sound modes in the second experimental run (top-to-bottom traces respectively). **(B)** Experimentally observed temporal decay of the vortex number with the corresponding uncertainties. **(C)** Evolution of the vortex dipole total kinetic energy (blue curve) and the free-vortex cluster kinetic energy (red curve). **(D)** Temporal dynamics of the angular momentum of vortex-cluster metastable states.

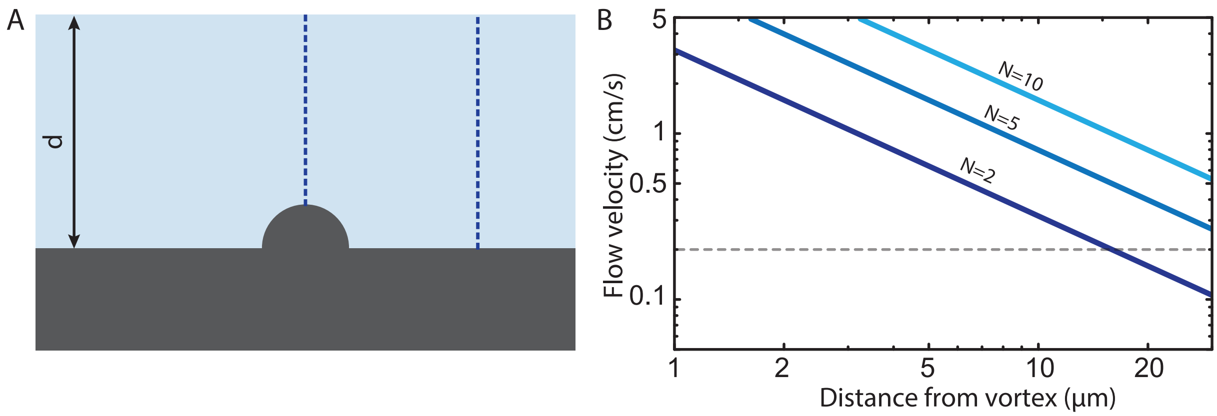

Figure S13: **(A)** A simplified model of pinning due to a hemispherical defect in a thin film of superfluid helium of thickness d. The vortex located on the defect (central dashed line) has less kinetic energy than one off the defect (right), due to its reduced length. **(B)** Background flow velocity induced by N circulation quanta trapped around the pedestal, versus radial offset from the disk center. The horizontal line indicates a flow velocity of $0.2\,\mathrm{cm/s}$.

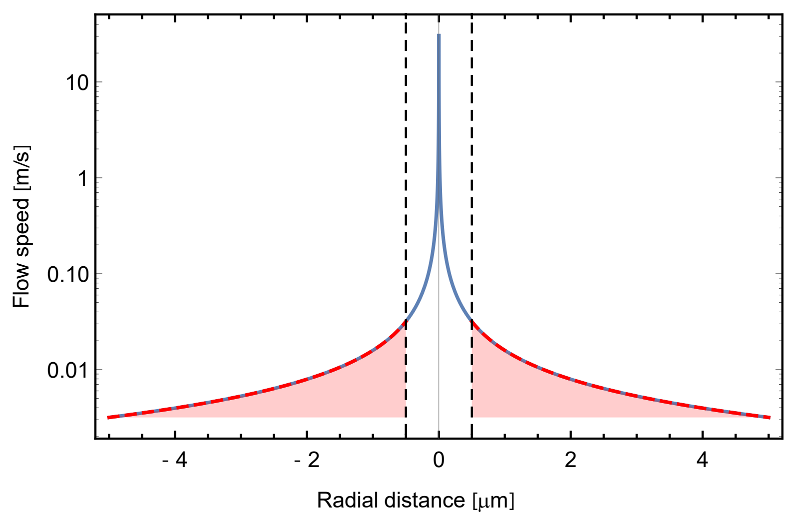

Figure S14: Superfluid flow velocity as a function of the radial distance from the core, for a single circulation quantum $\kappa = h/m_4 = 9.98 \times 10^{-8}$ m^{-2}s^{-1} (blue line). By clipping the high-velocity component of the flow field, quantized circulation around the micron-sized microtoroid pedestal (materialized by vertical dashed gray lines), is energetically favourable.

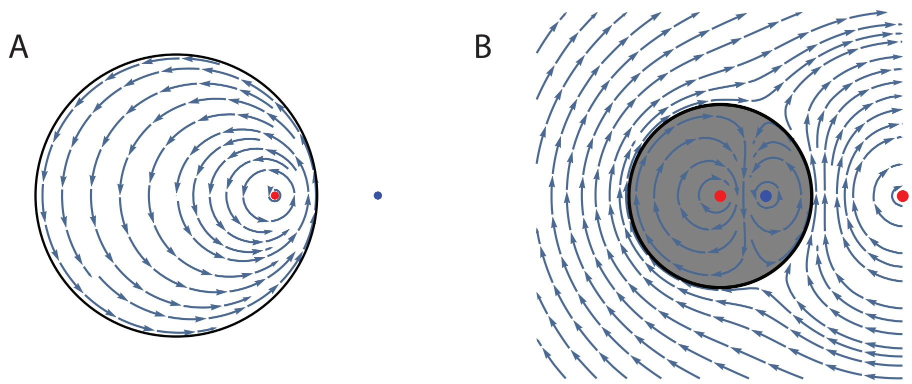

Figure S15: **(A)** Flow streamlines of a point vortex (red dot) offset from the center inside a circular domain (black circle). The no-flow boundary condition is enforced by the presence of an opposite signed image-vortex outside the boundary (blue dot) (79). **(B)** Flow streamlines of a point vortex (rightmost red dot) outside a cylindrical obstacle (gray disk) in a 2D plane. The no-flow boundary condition is enforced by an opposite signed image-vortex inside the obstacle (blue dot) and a same-signed image vortex in the center of the obstacle (left red dot).

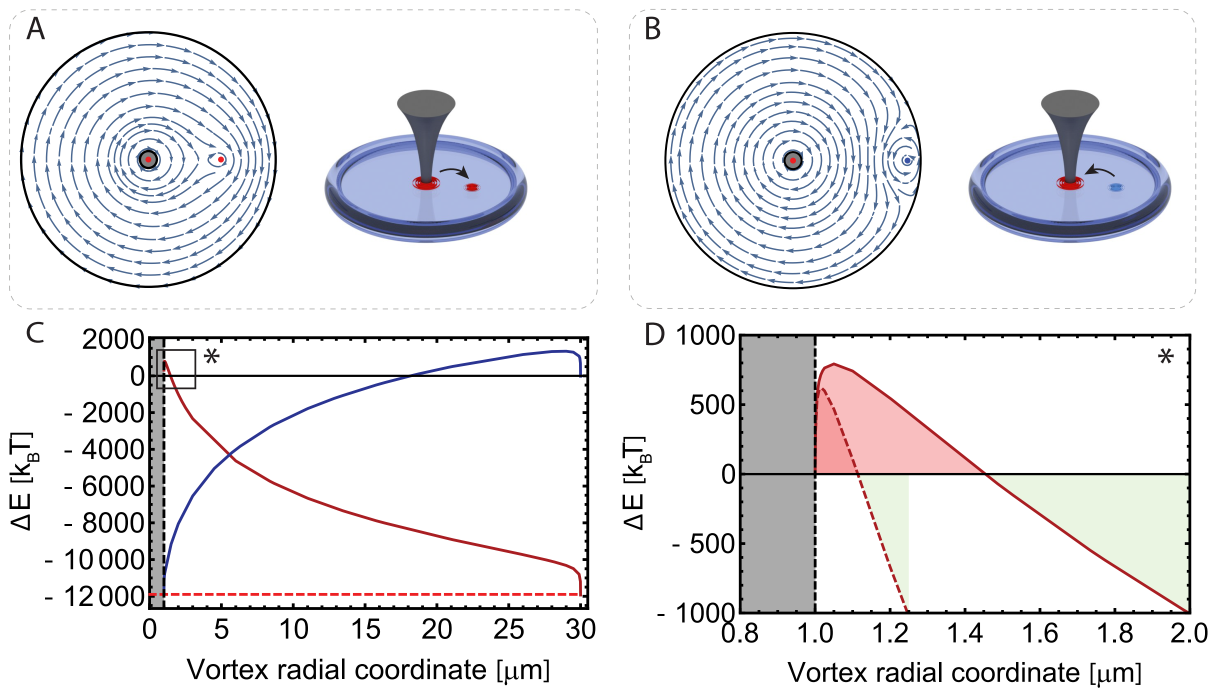

Figure S16: Two alternate decay scenarios for a large ($\kappa \gg 1$) circulation trapped around the device pedestal. **(A)** Positive vortex (red) exiting the large positive pinned circulation around the central pedestal (greyed-out region). Blue arrows display the flow streamlines calculated from Eq. (S17). **(B)** Incoming negative vortex (blue) annihilating with the positive circulation on the device pedestal. **(C)** Calculated kinetic energy cost of the decay processes illustrated in (A) and (B), starting from a positive circulation of $11 \times \kappa$ around the pedestal. (red curve: escaping positive vortex; blue curve: incoming negative vortex). The dashed red line marks the theoretical energy drop from the removal of one circulation quantum. **(D)** Zoom-in of the region marked by an asterisk '*' in (C), highlighting the potential barrier for the shedding of positive vortices. Solid red line and dashed red line show the potential barriers starting from a positive circulation of $11 \times \kappa$ and $31 \times \kappa$ around the pedestal respectively. Greyed out region marks the location of the pedestal.

Mode	$f_{\rm disk}$ (Hz)	$f_{\rm annulus}$ (Hz)	$\Delta f_{\rm disk}$ (Hz)	$\Delta f_{\rm annulus}$ (Hz)	$f_{\rm error}$ (%)	$\Delta f_{\rm error}$ (%)
(0,1)	57318	57426	-	-	0.19	-
(1,6)	269484	267301	193.3	188.3	0.81	2.6
(1,8)	363633	360127	261.8	256.7	0.96	1.95

Table S1: Comparison table for the eigenfrequencies and splitting in a disk vs annular geometry. Frequency and splitting values quoted for the eigenmodes of a 30 micron radius disk / a 30 micron outer radius annulus (see eigenmodes in Fig. S3). Frequency values are quoted for a 10 nm thick superfluid film. The frequency error ($f_{\rm error}$) and splitting error ($\Delta f_{\rm error}$) are typically quite small, below 3 %. Modes with $m = 0$ cannot be decomposed in the basis of clockwise and counter-clockwise rotating modes and experience therefore no splitting.

References and Notes

1. D. Mitra, P. T. Brown, E. Guardado-Sanchez, S. S. Kondov, T. Devakul, D. A. Huse, P. Schauß, W. S. Bakr, Quantum gas microscopy of an attractive Fermi–Hubbard system. *Nat. Phys.* **14**, 173–177 (2017). doi:10.1038/nphys4297

2. C. Gross, I. Bloch, Quantum simulations with ultracold atoms in optical lattices. *Science* **357**, 995–1001 (2017). doi:10.1126/science.aal3837 Medline

3. A. D. King, J. Carrasquilla, J. Raymond, I. Ozfidan, E. Andriyash, A. Berkley, M. Reis, T. Lanting, R. Harris, F. Altomare, K. Boothby, P. I. Bunyk, C. Enderud, A. Fréchette, E. Hoskinson, N. Ladizinsky, T. Oh, G. Poulin-Lamarre, C. Rich, Y. Sato, A. Y. Smirnov, L. J. Swenson, M. H. Volkmann, J. Whittaker, J. Yao, E. Ladizinsky, M. W. Johnson, J. Hilton, M. H. Amin, Observation of topological phenomena in a programmable lattice of 1,800 qubits. *Nature* **560**, 456–460 (2018). doi:10.1038/s41586-018-0410-x Medline

4. N. Chamel, Superfluidity and superconductivity in neutron stars. *J. Astrophys. Astron.* **38**, 43 (2017). doi:10.1007/s12036-017-9470-9

5. STAR Collaboration, Global Λ hyperon polarization in nuclear collisions. *Nature* **548**, 62–65 (2017). doi:10.1038/nature23004 Medline

6. P. W. Anderson, N. Itoh, Pulsar glitches and restlessness as a hard superfluidity phenomenon. *Nature* **256**, 25–27 (1975). doi:10.1038/256025a0

7. P. K. Kovtun, D. T. Son, A. O. Starinets, Viscosity in strongly interacting quantum field theories from black hole physics. *Phys. Rev. Lett.* **94**, 111601 (2005). doi:10.1103/PhysRevLett.94.111601 Medline

8. P. W. Adams, W. I. Glaberson, Vortex dynamics in superfluid helium films. *Phys. Rev. B* **35**, 4633–4652 (1987). doi:10.1103/PhysRevB.35.4633 Medline

9. J. M. Kosterlitz, D. J. Thouless, *J. Phys. Chem.* **5**, L124–L126 (1972).

10. D. J. Bishop, J. D. Reppy, Study of the superfluid transition in two-dimensional He 4 films. *Phys. Rev. Lett.* **40**, 1727–1730 (1978). doi:10.1103/PhysRevLett.40.1727

11. T. W. Neely, A. S. Bradley, E. C. Samson, S. J. Rooney, E. M. Wright, K. J. H. Law, R. Carretero-González, P. G. Kevrekidis, M. J. Davis, B. P. Anderson, Characteristics of two-dimensional quantum turbulence in a compressible superfluid. *Phys. Rev. Lett.* **111**, 235301 (2013). doi:10.1103/PhysRevLett.111.235301 Medline

12. P. Wiegmann, A. G. Abanov, Anomalous hydrodynamics of two-dimensional vortex fluids. *Phys. Rev. Lett.* **113**, 034501 (2014). doi:10.1103/PhysRevLett.113.034501 Medline

13. D. V. Freilich, D. M. Bianchi, A. M. Kaufman, T. K. Langin, D. S. Hall, Real-time dynamics of single vortex lines and vortex dipoles in a Bose-Einstein condensate. *Science* **329**, 1182–1185 (2010). doi:10.1126/science.1191224 Medline

14. S. Donadello, S. Serafini, M. Tylutki, L. P. Pitaevskii, F. Dalfovo, G. Lamporesi, G. Ferrari, Observation of solitonic vortices in Bose-Einstein condensates. *Phys. Rev. Lett.* **113**, 065302 (2014). doi:10.1103/PhysRevLett.113.065302 Medline

15. A. Amo, S. Pigeon, D. Sanvitto, V. G. Sala, R. Hivet, I. Carusotto, F. Pisanello, G. Leménager, R. Houdré, E. Giacobino, C. Ciuti, A. Bramati, Polariton superfluids reveal quantum hydrodynamic solitons. *Science* **332**, 1167–1170 (2011). doi:10.1126/science.1202307 Medline

16. E. Estrecho, T. Gao, N. Bobrovska, M. D. Fraser, M. Steger, L. Pfeiffer, K. West, T. C. H. Liew, M. Matuszewski, D. W. Snoke, A. G. Truscott, E. A. Ostrovskaya, Single-shot condensation of exciton polaritons and the hole burning effect. *Nat. Commun.* **9**, 2944 (2018). doi:10.1038/s41467-018-05349-4 Medline

17. G. Gauthier, M. T. Reeves, X. Yu, A. S. Bradley, M. A. Baker, T. A. Bell, H. Rubinsztein-Dunlop, M. J. Davis, T. W. Neely, Giant vortex clusters in a two-dimensional quantum fluid. *Science* **364**, 1264–1267 (2019). doi:10.1126/science.aat5718 Medline

18. S. P. Johnstone A. J. Groszek, P. T. Starkey, C. J. Billington, T. P. Simula, K. Helmerson. *Science* **364**, 1267–1271 (2019).

19. L. Onsager, Statistical hydrodynamics. *Nuovo Cim.* **6** (S2), 279–287 (1949). doi:10.1007/BF02780991

20. P. Makotyn, C. E. Klauss, D. L. Goldberger, E. A. Cornell, D. S. Jin, Universal dynamics of a degenerate unitary Bose gas. *Nat. Phys.* **10**, 116–119 (2014). doi:10.1038/nphys2850

21. M. W. Zwierlein, J. R. Abo-Shaeer, A. Schirotzek, C. H. Schunck, W. Ketterle, Vortices and superfluidity in a strongly interacting Fermi gas. *Nature* **435**, 1047–1051 (2005). doi:10.1038/nature03858 Medline

22. C. Eigen, J. A. P. Glidden, R. Lopes, E. A. Cornell, R. P. Smith, Z. Hadzibabic, Universal prethermal dynamics of Bose gases quenched to unitarity. *Nature* **563**, 221–224 (2018). doi:10.1038/s41586-018-0674-1 Medline

23. B. Ko, J. W. Park, Y. Shin, *Nat. Phys.* (2019). 10.1038/s41567-019-0650-1

24. E. Fonda, D. P. Meichle, N. T. Ouellette, S. Hormoz, D. P. Lathrop, Direct observation of Kelvin waves excited by quantized vortex reconnection. *Proc. Natl. Acad. Sci. U.S.A.* **111** (Suppl 1), 4707–4710 (2014). doi:10.1073/pnas.1312536110 Medline

25. H. Hu, B. C. Mulkerin, U. Toniolo, L. He, X.-J. Liu, Reduced quantum anomaly in a quasi-two-dimensional Fermi superfluid: Significance of the confinement-induced effective range of interactions. *Phys. Rev. Lett.* **122**, 070401 (2019). doi:10.1103/PhysRevLett.122.070401 Medline

26. F. Ancilotto, M. Barranco, F. Coppens, J. Eloranta, N. Halberstadt, A. Hernando, D. Mateo, M. Pi, Density functional theory of doped superfluid liquid helium and nanodroplets. *Int. Rev. Phys. Chem.* **36**, 621–707 (2017). doi:10.1080/0144235X.2017.1351672

27. D. J. Thouless, J. R. Anglin, Vortex mass in a superfluid at low frequencies. *Phys. Rev. Lett.* **99**, 105301 (2007). doi:10.1103/PhysRevLett.99.105301 Medline

28. T. Simula, Vortex mass in a superfluid. *Phys. Rev. A (Coll. Park)* **97**, 023609 (2018). doi:10.1103/PhysRevA.97.023609

29. E. B. Sonin, Magnus force in superfluids and superconductors. *Phys. Rev. B* **55**, 485–501 (1997). doi:10.1103/PhysRevB.55.485

30. L. Thompson, P. C. E. Stamp, Quantum dynamics of a Bose superfluid vortex. *Phys. Rev. Lett.* **108**, 184501 (2012). doi:10.1103/PhysRevLett.108.184501 Medline

31. G. I. Harris, D. L. McAuslan, E. Sheridan, Y. Sachkou, C. Baker, W. P. Bowen, Laser cooling and control of excitations in superfluid helium. *Nat. Phys.* **12**, 788–793 (2016). doi:10.1038/nphys3714

32. A. Kashkanova, A. B. Shkarin, C. D. Brown, N. E. Flowers-Jacobs, L. Childress, S. W. Hoch, L. Hohmann, K. Ott, J. Reichel, J. G. E. Harris, Superfluid Brillouin optomechanics. *Nat. Phys.* **13**, 74–79 (2016). doi:10.1038/nphys3900

33. A. Noury, J. Vergara-Cruz, P. Morfin, B. Plaçais, M. C. Gordillo, J. Boronat, S. Balibar, A. Bachtold, Layering Transition in Superfluid Helium Adsorbed on a Carbon Nanotube Mechanical Resonator. *Phys. Rev. Lett.* **122**, 165301 (2019). doi:10.1103/PhysRevLett.122.165301 Medline

34. K. A. Gillis, S. M. Volz, J. M. Mochel, Velocity-dependent dissipation from free vortices and bound vortex pairs below the Kosterlitz-Thouless transition. *Phys. Rev. B* **40**, 6684–6694 (1989). doi:10.1103/PhysRevB.40.6684 Medline

35. D. K. Armani, T. J. Kippenberg, S. M. Spillane, K. J. Vahala, Ultra-high-Q toroid microcavity on a chip. *Nature* **421**, 925–928 (2003). doi:10.1038/nature01371 Medline

36. D. L. McAuslan, G. I. Harris, C. Baker, Y. Sachkou, X. He, E. Sheridan, W. P. Bowen, Microphotonic Forces from Superfluid Flow. *Phys. Rev. X* **6**, 021012 (2016). doi:10.1103/PhysRevX.6.021012

37. Materials and methods are available as supplementary materials.

38. M. T. Reeves, T. P. Billam, X. Yu, A. S. Bradley, Enstrophy cascade in decaying two-dimensional quantum turbulence. *Phys. Rev. Lett.* **119**, 184502 (2017). doi:10.1103/PhysRevLett.119.184502 Medline

39. S. Forstner, Y. Sachkou, M. Woolley, G. I. Harris, X. He, W. P. Bowen, C. G. Baker, Modelling of vorticity, sound and their interaction in two-dimensional superfluids. *New J. Phys.* **21**, 053029 (2019). doi:10.1088/1367-2630/ab1bb5

40. F. M. Ellis, H. Luo, Observation of the persistent-current splitting of a third-sound resonator. *Phys. Rev. B* **39**, 2703–2706 (1989). doi:10.1103/PhysRevB.39.2703 Medline

41. C. G. Baker, G. I. Harris, D. L. McAuslan, Y. Sachkou, X. He, W. P. Bowen, Theoretical framework for thin film superfluid optomechanics: Towards the quantum regime. *New J. Phys.* **18**, 123025 (2016). doi:10.1088/1367-2630/aa520d

42. F. M. Ellis, L. Li, Quantum swirling of superfluid helium films. *Phys. Rev. Lett.* **71**, 1577–1580 (1993). doi:10.1103/PhysRevLett.71.1577 Medline

43. M. S. Hanay, S. I. Kelber, C. D. O'Connell, P. Mulvaney, J. E. Sader, M. L. Roukes, Inertial imaging with nanomechanical systems. *Nat. Nanotechnol.* **10**, 339–344 (2015). doi:10.1038/nnano.2015.32 Medline

44. D. T. Ekholm, R. B. Hallock, Behavior of persistent currents under conditions of strong decay. *Phys. Rev. Lett.* **42**, 449–452 (1979). doi:10.1103/PhysRevLett.42.449

45. A. I. Golov, P. M. Walmsley, Homogeneous turbulence in superfluid 4He in the low-temperature limit: experimental progress. *J. Low Temp. Phys.* **156**, 51–70 (2009). doi:10.1007/s10909-009-9896-9

46. E. Kozik, B. Svistunov, Scanning superfluid-turbulence cascade by its low-temperature cutoff. *Phys. Rev. Lett.* **100**, 195302 (2008). doi:10.1103/PhysRevLett.100.195302 Medline

47. L. Yu, Vortex dynamics and persistent current decay in thin superfluid He 4 films. *Phys. Rev. B* **25**, 198–215 (1982). doi:10.1103/PhysRevB.25.198

48. G. Agnolet, D. F. McQueeney, J. D. Reppy, Kosterlitz-Thouless transition in helium films. *Phys. Rev. B* **39**, 8934–8958 (1989). doi:10.1103/PhysRevB.39.8934 Medline

49. S. Serafini, L. Galantucci, E. Iseni, T. Bienaimé, R. N. Bisset, C. F. Barenghi, F. Dalfovo, G. Lamporesi, G. Ferrari, Vortex reconnections and rebounds in trapped atomic Bose-Einstein condensates. *Phys. Rev. X* **7**, 021031 (2017). doi:10.1103/PhysRevX.7.021031

50. Y. P. Sachkou, C. G. Baker, G. I. Harris, Oliver R. Stockdale, Stefan Forstner, Matthew T. Reeves, Xin He, David L. McAuslan, Ashton S. Bradley, Matthew J. Davis, Warwick P. Bowen, Experimental and simulation datasets for: Coherent vortex dynamics in a strongly-interacting superfluid on a silicon chip, Version 1.0, Zenodo (2019); https://doi.org/10.5281/zenodo.3524827.

51. Y. P. Sachkou, C. G. Baker, G. I. Harris, Oliver R. Stockdale, Stefan Forstner, Matthew T. Reeves, Xin He, David L. McAuslan, Ashton S. Bradley, Matthew J. Davis, Warwick P. Bowen, Data processing and simulation scripts for: Coherent vortex dynamics in a strongly-interacting superfluid on a silicon chip, Version 1.0, Zenodo (2019); https://doi.org/10.5281/zenodo.3524872.

52. H. Lee, T. Chen, J. Li, K. Y. Yang, S. Jeon, O. Painter, K. J. Vahala, Chemically etched ultrahigh-Q wedge-resonator on a silicon chip. *Nat. Photonics* **6**, 369–373 (2012). doi:10.1038/nphoton.2012.109

53. C. Baker, W. Hease, D.-T. Nguyen, A. Andronico, S. Ducci, G. Leo, I. Favero, Photoelastic coupling in gallium arsenide optomechanical disk resonators. *Opt. Express* **22**, 14072–14086 (2014). doi:10.1364/OE.22.014072 Medline

54. T. J. Kippenberg, H. Rokhsari, T. Carmon, A. Scherer, K. J. Vahala, Analysis of radiation-pressure induced mechanical oscillation of an optical microcavity. *Phys. Rev. Lett.* **95**, 033901 (2005). doi:10.1103/PhysRevLett.95.033901 Medline

55. V. Ambegaokar, B. I. Halperin, D. R. Nelson, E. D. Siggia, Dissipation in two-dimensional superfluids. *Phys. Rev. Lett.* **40**, 783–786 (1978). doi:10.1103/PhysRevLett.40.783

56. V. Ambegaokar, B. I. Halperin, D. R. Nelson, E. D. Siggia, Dynamics of superfluid films. *Phys. Rev. B* **21**, 1806–1826 (1980). doi:10.1103/PhysRevB.21.1806

57. P. K. Newton, *The N-Vortex Problem: Analytical Techniques* (Springer Science & Business Media, 2013).

58. O. Bühler, Statistical mechanics of strong and weak point vortices in a cylinder. *Phys. Fluids* **14**, 2139–2149 (2002). doi:10.1063/1.1483305

59. D. Marchand, thesis, University of British Columbia (2006).

60. X. Yu, A. S. Bradley, Emergent non-Eulerian hydrodynamics of quantum vortices in two dimensions. *Phys. Rev. Lett.* **119**, 185301 (2017). doi:10.1103/PhysRevLett.119.185301 Medline

61. R. Hänninen, A. W. Baggaley, Vortex filament method as a tool for computational visualization of quantum turbulence. *Proc. Natl. Acad. Sci. U.S.A.* **111**, 4667–4674 (2014). doi:10.1073/pnas.1312535111 Medline

62. C. F. Barenghi, V. S. L'vov, P.-E. Roche, *Proc. Natl. Acad. Sci. U.S.A.* **111**, 201312548 (2014).

63. R. J. Donnelly, C. F. Barenghi, The Observed Properties of Liquid Helium at the Saturated Vapor Pressure. *J. Phys. Chem. Ref. Data* **27**, 1217–1274 (1998). doi:10.1063/1.556028

64. C. A. Jones, P. H. Roberts, *J. Phys. A* **15**, 2599–2619 (1982).

65. T. L. Ashbee, thesis, University College London (2014).

66. R. A. Smith, T. M. O'Neil, Nonaxisymmetric thermal equilibria of a cylindrically bounded guiding-center plasma or discrete vortex system. *Phys. Fluids B Plasma Phys.* **2**, 2961–2975 (1990). doi:10.1063/1.859362

67. B. Svistunov, E. Kozik, *Superfluid States of Matter* (CRC, 2015).

68. D. Browne, S. Doniach, Vortex pinning and the decay of persistent currents in unsaturated superfluid helium films. *Phys. Rev. B* **25**, 136–150 (1982). doi:10.1103/PhysRevB.25.136

69. K. W. Schwarz, Three-dimensional vortex dynamics in superfluid 4He: Line-line and line-boundary interactions. *Phys. Rev. B* **31**, 5782–5804 (1985). doi:10.1103/PhysRevB.31.5782 Medline

70. G. W. Stagg, N. G. Parker, C. F. Barenghi, Superfluid boundary layer. *Phys. Rev. Lett.* **118**, 135301 (2017). doi:10.1103/PhysRevLett.118.135301 Medline

71. R. J. Zieve, C. M. Frei, D. L. Wolfson, Energy loss from a moving vortex in superfluid helium. *Phys. Rev. B* **86**, 174504 (2012). doi:10.1103/PhysRevB.86.174504

72. K. W. Schwarz, Phase slip and turbulence in superfluid 4He: A vortex mill that works. *Phys. Rev. Lett.* **64**, 1130–1133 (1990). doi:10.1103/PhysRevLett.64.1130 Medline

73. S. K. Nemirovskii, Quantum turbulence: Theoretical and numerical problems. *Phys. Rep.* **524**, 85–202 (2013). doi:10.1016/j.physrep.2012.10.005

74. D. E. Zmeev, P. M. Walmsley, A. I. Golov, P. V. E. McClintock, S. N. Fisher, W. F. Vinen, Dissipation of Quasiclassical Turbulence in Superfluid ^4He. *Phys. Rev. Lett.* **115**, 155303 (2015). doi:10.1103/PhysRevLett.115.155303 Medline

75. R. J. Donnelly, *Quantized Vortices in Helium II* (Cambridge Univ. Press, 1991).

76. D. R. Tilley, J. Tilley, *Superfluidity and Superconductivity* (IOP Publishing, 1990).

77. R. J. Donnelly, A. L. Fetter, Stability of superfluid flow in an annulus. *Phys. Rev. Lett.* **17**, 747–750 (1966). doi:10.1103/PhysRevLett.17.747

78. A. L. Fetter, Low-lying superfluid states in a rotating annulus. *Phys. Rev.* **153**, 285–296 (1967). doi:10.1103/PhysRev.153.285

79. H. Lamb, *Hydrodynamics* (Cambridge Univ. Press, 1993).

80. M. Reeves, thesis, University of Otago (2017).